NEUTRON RADIATION EFFECTS ON Ge AND GeSn SEMICONDUCTORS

THESIS

Christopher T. O'Daniel, 2d Lt, USAF

AFIT-ENP-MS-16-M-077

DEPARTMENT OF THE AIR FORCE
AIR UNIVERSITY

AIR FORCE INSTITUTE OF TECHNOLOGY

Wright-Patterson Air Force Base, Ohio

DISTRIBUTION STATEMENT A
APPROVED FOR PUBLIC RELEASE; DISTRIBUTION UNLIMITED

The views expressed in this document are those of the author and do not reflect the official policy or position of the United States Air Force, the United States Department of Defense or the United States Government. This material is declared a work of the U.S. Government and is not subject to copyright protection in the United States.

AFIT-ENP-MS-16-M-077

NEUTRON RADIATION EFFECTS ON Ge AND GeSn SEMICONDUCTORS

THESIS

Presented to the Faculty

Department of Engineering Physics

Graduate School of Engineering and Management

Air Force Institute of Technology

Air University

Air Education and Training Command

in Partial Fulfillment of the Requirements for the

Degree of Master of Science

Christopher T. O'Daniel, BS

2d Lt, USAF

March 2016

DISTRIBUTION STATEMENT A
APPROVED FOR PUBLIC RELEASE; DISTRIBUTION UNLIMITED

AFIT-ENP-MS-16-M-077

NEUTRON RADIATION EFFECTS ON Ge AND GeSn SEMICONDUCTORS

THESIS

Christopher T. O'Daniel, BS
2d Lt, USAF

Committee Membership:

Dr. Yung Kee Yeo
Chair

Lt Col Michael Hogsed, PhD
Member

AFIT-ENP-MS-16-M-077

Abstract

Two different semiconductor materials received neutron radiation for assessment of radiation damage. The two materials are undoped bulk Ge and epitaxial $Ge_{0.991}Sn_{0.009}$, which is doped heavily with phosphorous. At room temperature, the Ge sample has direct and indirect bandgaps at 0.78 eV and 0.66 eV, respectively. The $Ge_{0.991}Sn_{0.009}$ sample has direct and indirect bandgaps at 0.72 eV and 0.63 eV, respectively. Two samples of each material were exposed to research reactor neutrons, delivering a 1 MeV equivalent neutron fluence of $2.52 \times 10^{15}\ \frac{n}{cm^2}$. In order to assess the radiation damage and recovery, photoluminescence (PL) measurements were taken before and after irradiation weekly. The Ge experienced heavy neutron radiation damage, decreasing the direct and indirect bandgap PL intensity to about 4% and 1%, respectively, from the pre-neutron irradiation value. Room temperature annealing of the Ge sample over four weeks brought the recovery of the direct and indirect bandgap PL intensities only to about 7% and 3%, while an accumulated 60 $°C$ annealing for 100 minutes brought the PL recoveries to about 11% and 3%, respectively. The $Ge_{0.991}Sn_{0.009}$ sample experienced neutron damage that decreased the direct bandgap PL intensity to about 37% of the pre-neutron irradiation PL intensity. The direct bandgap PL intensities recovered to 88% and 86%, respectively after five weeks for a sample annealed only at room temperature and a sample that was also annealed at 60 $°C$ for 130 minutes. The significantly different radiation responses of bulk Ge and epitaxial $Ge_{0.991}Sn_{0.009}$ highlights that $GeSn$-based materials should be further researched for their neutron radiation hardness capabilities.

AFIT-ENP-MS-16-M-077

To the Chuckleheads.

If it was not for you, then this would have been very dull.

Acknowledgements

I would like to thank Dr. Yung Kee Yeo for his support and guidance and Lt Col Hogsed for his assistance on this thesis. For constant assistance in the laboratory, I would like to thank Dr. Buguo Wang, and the lab technicians, Greg Smith and Michael Ranft. My appreciation extends to Professor John Kouvetakis of Arizona State University for growing the samples which are used for these experiments, and Ohio State University for use of their Neutron Reactor for irradiation purposes.

Christopher T. O'Daniel

Table of Contents

Page

Abstract iv

Acknowledgements vi

List of Figures ix

List of Tables xi

I. Introduction 1

1.1 Objectives 1
1.2 Motivation 2
1.3 Problem Statement 2
1.4 Background 3
Silicon 3
Silicon and Germanium 3
Germanium Tin 4
1.5 Sponsorship and Partnership 5

II. Theory 6

2.1 Semiconductor 6
Band Structure 6
Density of States 7
Charge Carrier Distribution 8
2.2 Photoluminescence 11
2.3 Neutron Radiation 14
Neutron Elastic Scattering 15

III. Samples and Experiment Setup 20

3.1 Samples 20
3.2 Photoluminescence 20
3.3 Neutron Radiation 22
3.4 Annealing 23

IV. Results and Analysis 25

4.1 Pre-Characterization 25
4.2 Ge Wafer 25
4.3 $Ge_{0.991}Sn_{0.009}$ 35

Page

V. Future Work 47

5.1 Alternate Radiation Types 47
5.2 Alternate Sn contents 48
5.3 In situ above RT annealing 48
5.4 Electrical Properties 49

VI. Conclusions 50

Appendix A. LakeShore 7704A Hall-Effect Measurement System 52

Appendix B. Photoluminescence System 55

2.1 Argon Ion Laser [1] 55
2.2 Ti-Sapphire Laser [1] 57
2.3 Preamplifier [2] 58
2.4 LakeShore 336 Temperature Controller [3] 60
2.5 F-70 Water-Cooled Compressor [4] 62

Appendix C. Annealing System 63

Bibliography 64

List of Figures

Figure Page

1 Band diagram, density of states, Fermi function, and carrier concentration for an n-type semiconductor at room temperature. 10

2 Elastic collision diagram 16

3 Elastic collision relating velocities of two systems 17

4 Photoluminescence setup 21

5 Annealing tube furnace 24

6 Photoluminescence representation of neutron radiation damage 26

7 Ge sample room temperature photoluminescence comparison of original signal and one week post neutron radiation 27

8 Ge sample bandgap growth over four weeks after neutron radiation. 29

9 Ge sample post neutron irradiation photoluminescence comparison between room temperature annealed and 60 $°C$ annealed sample. 30

10 Ge sample photoluminescence comparison of annealed samples after four weeks. 32

11 Ge sample bandgap extrapolation 34

12 Ge sample photoluminescence comparison of 60 $°C$ annealed samples after four weeks with pre-neutron radiation photoluminescence. 35

13 $Ge_{0.991}Sn_{0.009}$ room temperature photoluminescence comparison of original signal and one week post neutron radiation 37

14 $Ge_{0.991}Sn_{0.009}$ room temperature photoluminescence comparison of original signal and the two weeks post neutron radiation 38

Figure Page

15 $Ge_{0.991}Sn_{0.009}$ room temperature photoluminescence comparison of original signal and three weeks post neutron radiation 39

16 $Ge_{0.991}Sn_{0.009}$ room temperature photoluminescence comparison of original signal and four weeks post neutron radiation 40

17 $Ge_{0.991}Sn_{0.009}$ room temperature photoluminescence comparison of original signal and five weeks post neutron radiation 41

18 $Ge_{0.991}Sn_{0.009}$ post neutron irradiation PL comparison between RT annealed and 60 $°C$ annealed sample. 43

List of Tables

Table Page

1 The characteristics of a neutron. 14

2 Semiconductor material energy values. 19

3 Description of the two samples used in this study. 20

4 Bandgap photoluminescence extrapolation for Ge sample 33

NEUTRON RADIATION EFFECTS ON Ge AND GeSn SEMICONDUCTORS

I. Introduction

1.1 Objectives

The Department of Defense (DoD) has particular interest in infrared (IR) and optoelectronic devices due to their role in enhancing communications and other mission capabilities. The devices' operating environments are also of interest. Performance in high-radiation environments, including those resulting from an ever-growing nuclear threat and those present in outer space, is becoming increasingly relevant to device operations. For this reason, optoelectronic devices operating in the $1.3-1.6\,\mu m$ wavelength range are a focus for current research [5]. Preliminary results of Si-Ge-Sn and Ge-Sn alloys demonstrate the desired optical responses in the infra-red (IR) telecom regime [6]. However, these materials are not currently well-characterized. This means that before device fabrication can begin, systematic studies of the materials must be accomplished.

The objective of this study is to investigate the effects of neutron radiation upon the optical characteristics of the Ge-Sn and Ge alloys. In particular, this includes characterizing the annealing processes of the alloys in order to determine the length of time required to recover the original device characteristics after irradiation. Both controlled-heat annealing and room-temperature annealing were tested to determine which technique allowed for a faster recovery process. The optical characterizations were carried out by photoluminescence (PL) measurements.

1.2 Motivation

Electronic devices are an integral part of almost all Department of Defense missions. These missions require communication devices, Global Positioning System (GPS), and many other electronic devices to operate. Many of these devices also need to operate in high radiation environments that are not friendly to electronic systems. The DoD also rely on satellites that operate using optoelectronic devices. Radiation damage to electronics in space is of particular concern due to the near inability to change out any parts. Therefore, radiation-hard materials are needed for these environments. In addition to the characterization of the radiation hardness, quantifying how quickly and how complete annealing takes place to recover the original operating characteristics of the material is desired.

While in operation, a damaged device that is in space should be able to be fixed remotely without damaging other parts. This research for neutron irradiated Ge and GeSn samples looks into the effects of room temperature annealing and slightly elevated temperature annealing ($60°C$) that would not damage any of the devices but allow for increased speed in the damage annealing process. This would allow for methods for radiation-damaged optoelectronic devices in space to repair.

1.3 Problem Statement

This research seeks to show that GeSn material is a strong alternative as a Si- and Ge- based semiconductor material for use in high neutron radiation environments. This research will establish the importance of continuing research on this material for future use and integration into silicon-based devices. In addition, this research will look into increasing the annealing process by slightly elevating the annealing temperature. This will look into the benefit of adding a heat pad in integrated systems for improved annealing without having to change out components.

1.4 Background

Silicon.

Currently, most electronic devices are constructed from silicon because it is inexpensive and well-characterized for device applications. However, the field of microelectronics is drawing closer to the size reduction, bandwidth, and technological limits of the material. Many potential solutions have been researched, including the use of waveguides, electro-optic modulators, and optical switches. These methods have made progress. However, they do not fully resolve the most difficult fundamental challenge in the use of indirect bandgap materials in developing efficient light emitting sources [7].

Silicon and Germanium.

Germanium- and silicon-based semiconductors can be made to create direct bandgap semiconductor devices. This is a highly sought-after quality, because fundamental indirect bandgap materials are poor light emitters. In addition, this completely changes optical component integration in silicon electronics on a single chip. Germanium has a much smaller energy difference between the direct and indirect bandgap in comparison to silicon. Silicon has an indirect bandgap of 1.12 eV and a direct bandgap of 3.40 eV, providing a difference of 2.28 eV. Germanium has an indirect bandgap of 0.66 eV and a direct bandgap of 0.8 eV for a difference of 0.14 eV [8].

There are several known methods for reducing the difference between the direct and indirect bandgap, which is also referred to as the $\Gamma - L$ conduction valley separation. Tensile strain was the predominant method for many years, replacing the compressive strain that made poor crystalline structures. Germanium was predicted to become a direct bandgap under 2.0% tensile strain. One method for doing this involves growing germanium on silicon. This causes a 4% lattice constant mismatch

between the two layers. Because silicon has a smaller lattice distance than germanium, this creates a natural compressive strain on the germanium layer. The process of making device quality materials requires annealing them at high temperatures ($600 - 650°C$), which creates large thermal expansion, and letting them cool thereby creating tensile strain on the material [9]. Another method for creating a more direct bandgap emission involves increasing the n-type doping of germanium. Raising the doping to greater than $10^{19}\,cm^{-3}$ increases the Fermi level above the $L - valley$ in the conduction band. This shift in the conduction band allows for partial filling of the band with electrons. This then allows spill-over of electrons into the $\Gamma - valley$ from thermalization and increases the probability of direct recombination of holes with electrons. This recombination would be enhanced with electrical injection or photo-excitation. This process has indeed increased the PL from the direct-gap transition for the n-type doped Ge-on-Si layers. In addition, this led to an optically pumped laser [10].

Germanium Tin.

It is difficult to achieve the percentages needed to create a controllable direct bandgap material with tensile strain alone. Tin doping is an attractive alternative to the use of tensile strain that has proven to have similar results, in terms of reducing the $\Gamma - L$ conduction valley separation. A tin content of 1% is approximately equivalent to 0.35% tensile strain. Originally, creating a direct-bandgap material was predicted to require doping with 20% tin. However, it has been found that a crossover to a direct bandgap instead occurs at $6 - 9\%$ tin content [9]. This indicates that there is a bowing parameter for the direct transition instead of a linear progression. Like germanium, the combination of germanium-tin can also be grown on a silicon substrate. This would allow for integration into existing silicon-based devices.

In addition, this creates a dual modifier to the direct bandgap crossover. Both tensile strain between the germanium-tin and silicon and the tin doping in the germanium can exist in this configuration. This allows for a tunable device. The decoupling of the lattice constants allows for previously unattainable flexibility in bandgap and strain to be feasible and controllable.

1.5 Sponsorship and Partnership

This research is sponsored by Air Force Office of Science Research (AFOSR) and is accomplished in partnership with Arizona State University, where the materials are grown. The Ohio State University Nuclear Reactor Lab was utilized for sample irradiation.

II. Theory

2.1 Semiconductor

The usefulness of a semiconductor is its ability to operate as either an insulator or a conductor under specific conditions. These conditions include three primary topics: band structure, density of states, and charge carrier distribution. These topics will be investigated by the processes of PL.

Band Structure.

Semiconductor band structure is based upon a quantum treatment of each wave function throughout the entire lattice. This problem is highly complex, but this complexity is functionally reduced by using approximations and theorems to simplify the derivation. After the use of the tight binding approximation and Bloch's theorem, the total energy of the lattice can be described with equation (1) [11].

$$E = E_0 - \alpha - \gamma \sum_{j \neq j' \neq j''} \mathrm{e}^{ik(R_j - R_{j'})}. \tag{1}$$

Here, E_0 is the initial energy and α is the term for the nearest neighbors. The next-nearest neighbors are accounted for by the summation. The various sites in the lattice are accounted for by the j index. The tight binding approximation allows the next-nearest neighbors to be the most distant influential factors that must be evaluated. This allows for computation of the system's eigenvalues, from which the expected energy values can be found.

Leman demonstrates the use of this function in performing the calculations for the column IV atom electron configurations for diamond structure cubic crystals [12]. He shows that there are six bands, with theoretical energy gap given by equation (2) compared to the experimental observation shown in equation (3).

$$E_g = 2E_c - 5\ (eV) \tag{2}$$

$$E_g = 1.85E_c - 5.36\ (eV), \tag{3}$$

and where E_c is the cohesive energy and the bandgap is E_g. Comparing these equations lends validity to the approximation method.

Density of States.

The density of states is the number of states per unit volume in a specific energy range. This can be looked at in different spaces; however, the momentum space will be used for this example. A spherical energy surface with constant energies of $\epsilon + \mathrm{d}\epsilon$ is assumed. The surface can now be described as shown in equation (4).

$$p_x^2 + p_y^2 + p_z^2 = 2m^*\epsilon. \tag{4}$$

The momentum values in the x, y, and z direction are p_x, p_y, and p_z. The electron effective mass, m^*, is also used. The volume of the surface is given in equation (5).

$$\mathrm{d}V_p = 4\pi p^2 \mathrm{d}p. \tag{5}$$

Equation (4) is then substituted into equation (5).

$$\mathrm{d}V_p = 4\pi m^* \sqrt{2m^*\epsilon}\mathrm{d}\epsilon. \tag{6}$$

From here the density of states can be described as shown in equations (7) and (8).

$$\frac{\mathrm{d}V_p}{V_p} = \frac{4\pi m^* \sqrt{2m^*\epsilon}}{h^3/2V}. \tag{7}$$

$$\text{and } g(\epsilon)\mathrm{d}\epsilon = \frac{8\sqrt{2}\pi V m^{*\frac{3}{2}}\sqrt{\epsilon}}{h^3}\mathrm{d}\epsilon. \tag{8}$$

Equation (8) describes the density of states in three dimensions. This can also be performed in two dimensions by using a change in area $\mathrm{d}A_p$ instead of a change in volume $\mathrm{d}V_p$. The area of the surface is then given by equation (9).

$$\mathrm{d}A_p = 2\pi m^* \mathrm{d}\epsilon. \tag{9}$$

After going through the same process again, as in the three dimensional case, the density of states is obtained as shown in equation (10).

$$g(\epsilon)\mathrm{d}\epsilon = \frac{4\pi m^* A}{h^2}\mathrm{d}\epsilon. \tag{10}$$

Finally, this can also be done in one dimension through the same process. Equation (11) gives the density of states in one dimension.

$$g(\epsilon)\mathrm{d}\epsilon = \frac{1}{h}\sqrt{\frac{2m^*}{\epsilon}}\mathrm{d}\epsilon. \tag{11}$$

Density of states of materials are essential when determining the low energy limits of experiments (luminescence and absorption), band-to-band transitions, and Hall-effect analysis [13].

Charge Carrier Distribution.

There are multiple distribution functions that can be used to describe the distribution of electrons in a semiconductor; however, for thermal equilibrium, the best function to use is the Fermi-Dirac distribution, f_e, shown in equation (12).

$$f_e(E) = \frac{1}{\mathrm{e}^{\frac{E-E_f}{kT}} + 1}. \tag{12}$$

- k is Boltzmann's constant
- T is the temperature
- E_f is the Fermi level

The Fermi level, at $0\,K$, is located near the center of the bandgap for intrinsic semiconductors. Just as equation (12) refers to electrons, as noted by the subscript e, there is a corresponding equation for holes.

$$f_h(E) = 1 - f_e(E). \tag{13}$$

The concentration of charge carriers is found by multiplying the distribution function and the density of states and integrating the result, giving equation (14).

$$\int N(\epsilon)\mathrm{d}\epsilon = \int f(\epsilon)g(\epsilon)\mathrm{d}\epsilon. \tag{14}$$

There is a difference in the distribution of charge carriers in both n- and p-doped semiconductors. Variance in temperatures are the largest variable change in determining the Fermi energy level. The change in the Fermi energy level for both dopant types are shown in equation (15). The top equation refers to the donor or n-doped semiconductor, while the bottom refers to the acceptor or p-doped semiconductor [14].

$$\begin{aligned} E_f &= E_i + kT\ln\left(\frac{N_D}{N_i}\right) \qquad \text{where} \quad N_D \gg N_A,\ N_D \gg n_i, \\ E_f &= E_i - kT\ln\left(\frac{N_A}{N_i}\right) \qquad \text{where} \quad N_A \gg N_D,\ N_A \gg n_i. \end{aligned} \tag{15}$$

- E_f is the Fermi level

- E_i is the intrinsic Fermi level
- k is the Boltzmann's constant
- T is the temperature
- N_D is the total number of donors/cm^3
- N_A is the total number of acceptors/cm^3
- n_i is the intrinsic carrier concentration

Figure 1 shows the progression from the band structure to the density of states. The Fermi function is then convolved with the density of states to give the carrier concentration.

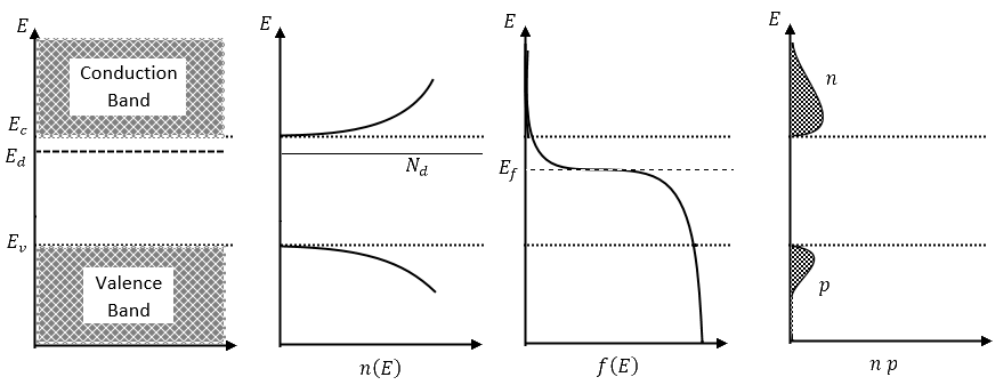

Figure 1. An n-type semiconductor at room temperature. This shows, from left to right, the band diagram, the density of states, the Fermi function, and the carrier concentration as a function of energy.

2.2 Photoluminescence

Photoluminescence is an important experiment for gaining insight into the purity and crystalline quality of a material. Photons of a wavelength above bandgap are absorbed and particular photons are re-emitted. Therefore, an analysis of photoluminescence scans the photons emitted from the material at each wavelength and examines their intensity to determine how much radiative recombination occurs at that frequency. The material plays a role in how the interactions occur [15].

For direct bandgap materials, a photon of higher energy than the bandgap is absorbed in the material, causing an electron-hole pair to be created. Although the election-hole pair can have a non-radiative transition in the material, it is possible for radiative recombination to occur, emitting a photon with a longer wavelength. It is most probable for the excited electron to recombine into one of three different hole states: the light hole band, heavy hole band, and split-off band [16]. The direct transition is the most efficient transition.

The indirect bandgap materials undergo a much different process. The photoluminescence process is much less probable in an indirect bandgap material than a direct bandgap material. The difference is that in order for radiative transition to occur, conservation of momentum must hold true, requiring usually simultaneous either phonon emission or absorption. For materials that have a high population of charge carriers in the indirect compared to the direct bandgap, the luminescence can still be stronger for the indirect than the direct, but the efficiency is much less [17].

Phonons have different modes associated with them. There are six possibilities: two transverse acoustic modes, two transverse optical modes, and an optical and acoustic longitudinal mode. The average energy for a phonon is related to the Debye temperature, which is a material property [18]. The Debye model estimates the phonon contribution based on the specific heat of the material. Equation (16) shows

the average phonon energy.

$$\epsilon_{av} = \frac{2}{3}k\Theta. \tag{16}$$

- k is Boltzmann's constant
- Θ is the Debye temperature.

The Debye temperature for germanium is 378 K, which makes the average phonon energy 21 meV.

The value of the band-to-band transition intensity can be calculated based on quantum transition probability, density of states, and charge carrier concentration. The approximation for this intensity is shown in equation (17).

$$I \approx |M|^2 g(h\nu)N(h\nu). \tag{17}$$

- M is the quantum mechanical transition probability
- $g(h\nu)$ is the density of states at energy $E = h\nu$
- $N(h\nu)$ is the concentration of charge carriers at energy $E = h\nu$

From here, there are a few possibilities based on the material. If the material is a direct gap material with a low enough charge carrier concentration, then the Maxwell-Boltzmann approximation can be used for the distribution function, giving the intensity in equation (18).

$$I = C(\epsilon - \epsilon_g)^{\frac{1}{2}}\, \mathrm{e}^{\frac{\epsilon-\epsilon_g}{kT}}. \tag{18}$$

- ϵ_g is the bandgap energy
- C is the proportionality constant

- T is the temperature
- k is Boltzmann's constant

This allows for the solving of the luminescence peak. This is done by solving for ϵ_g, in equation (18), by taking the derivative and setting it equal to zero. This results in a luminescence peak of $\epsilon_{peak} = \epsilon_g + \frac{kT}{2}$.

When the material is a degenerate semiconductor equation (18) is more complicated due to the Maxwell Boltzmann approximation can no longer be used. This changes the Fermi energy for both the conduction and valence band. Now self-absorption affects are considered the intensity of luminescence. If the radiative recombination occurs uniformly inside the sample, the emitted intensity can be described as follows.

$$I_{se} = \frac{(1-R)I(1-\mathrm{e}^{-\alpha t})}{\alpha t}. \tag{19}$$

- R is the reflectance of the exit surface
- I is the emission spectrum from equation (18)
- α is the absorption coefficient
- t is the thickness of the sample

Equation (19) shows that a stronger sample absorption causes a more significantly reduced emission spectrum.

Radiative recombination can occur due to multiple additional factors. If there are impurities in the material, then the impurity atoms can ionize, causing an opposite charge force on the conduction band electrons, which pulls them in while applying a repulsive force to the valence band holes. In addition, vacancies, dislocations,

and boundaries also can lead to forms of radiative recombination. When looking at a p-type material, band-to-band recombination should show power dependence in luminescence due to the higher population of majority carriers (holes) compared to minority carriers (electrons). Therefore, as power increases, there is an increase in the minority carriers, creating a linear proportionality between intensity and excitation energy power.

2.3 Neutron Radiation

There are multiple places where radiation can be a serious problem. Outer space is a place where materials are under constant bombardment from a wide range of energies and types of cosmic radiation. In high altitude flights, the atmosphere has far fewer particles to interrupt the path of incoming radiation. This is an environment which is susceptible to high radiation. Other places include those located near nuclear reactors and materials, particle accelerators, and nuclear accidents or warfare.

Table 1. The characteristics of a neutron. This is in reference to neutrons ranging from thermal to fast neutrons. These values are calculated from room temperature.

	Symbol	Charge	Ionization	Mass (amu)	Velocity (cm/sec)	Range in Air
Neutron (n)	${}^{1}_{0}n$	neutral	Indirect	1.008665	1.38×10^9	$\approx 39250\,cm$

It is important to have semiconductor materials which are radiation hard. Extensive development and testing is needed for the production of radiation-tolerant electronic and optoelectric device designs. The materials also need to be characterized in terms of how they react to and recover from possible radiation damage. There are multiple tests that are done: total ionizing dose, enhanced low dose rate effects, neutron and proton displacement damage, and single event upsets. However, since current research is carried on a material instead of an integrated circuit, some of these tests will not be needed [19].

Neutron ionizing radiation comes primarily from indirect ionization. Because neutrons have no charge, they can free particles creating ions or initiate a nuclear transformation. The two fundamental interactions of neutrons are scattering and absorption [17, 20].

For neutron radiation, the primary effect which causes problems is lattice displacement. Lattice displacement takes place on a large number of atoms, which leads to an increased number of non-radiative recombination centers. Deep-level defects in the material are also created from this interaction. The material also reduces the lifetime of the minority carriers. The material sensitivity to radiation damage effects increases with integration into the system and by decreasing the size of materials [19, 21, 22].

Radiation effects can also cause activation in the materials by creating isotopes and decay chains. The neutrons can activate the tin to make it unstable; however, ten of thirteen tin isotopes are still stable. Germanium has five naturally occurring isotopes, four of which are stable. The fifth, ^{76}Ge, is slightly radioactive and decays by double beta decay with a half life of 1.78×10^{21} years. Silicon has four naturally occurring isotopes, three of which are stable. The last is a beta minus decay with a half-life of 153 years.

Neutron Elastic Scattering.

Since neutrons are electrically neutral, a collision with a nucleus results in elastic scattering. The probability of the neutron colliding with a lattice atom is based on the double differential scattering cross section.

$$\sigma(E_i, \Omega) = \int \sigma_s(E_i, E_f, \Omega)\, \mathrm{d}E_f. \tag{20}$$

- σ_s is the scattering cross section in terms of energy and angle.
- E_i is the incident energy of the neutron.

- E_f is the final energy of the neutron.

- Ω is the solid angle at which the neutron is scattered from the collision.

The important thing to look at is the energy transfer to the struck atom, as the displacement of this atom is what causes problems in the material. To do this, there are a few things that must be considered, such as conservation of momentum and kinetic energy [23]. There are two scenarios to consider for this application, which can be seen in Fig. 2 and are described in the following relation.

$$V_{CM} = \left(\frac{m}{M+m}\right) v_l. \tag{21}$$

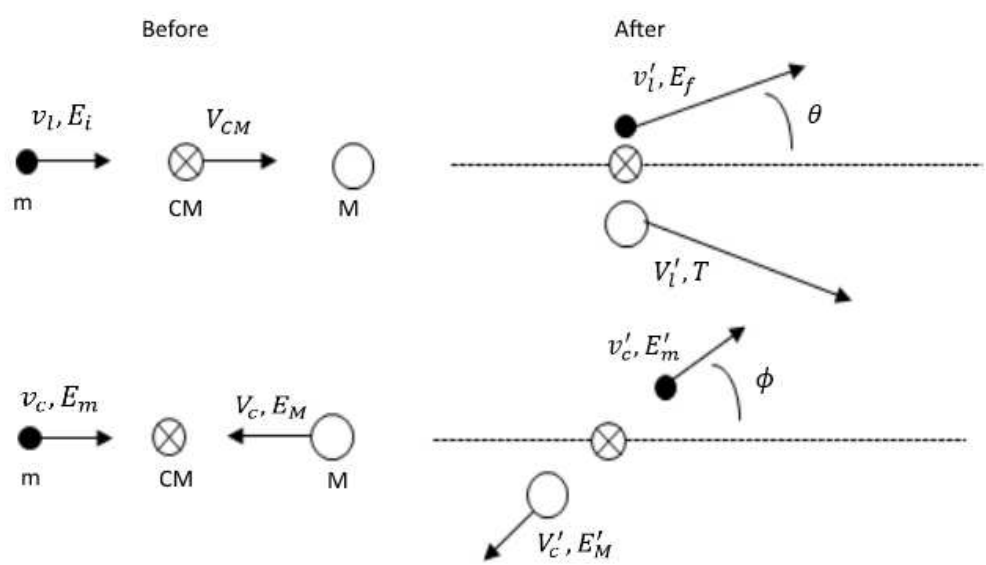

Figure 2. Elastic collision figure between neutron and atom. The top system is the laboratory setup, annotated by the l, while the bottom is the center of mass (CM) indicated by the c. For the laboratory system, the neutron of mass m has a velocity of v_l and initial energy of E_i. The velocity of the neutron ($v_l^{'}$) after scattering and the struck atom ($V_l^{'}$) with the kinetic energy transferred to the struck atom given by T. For the CM system, the neutron of mass m has a velocity of v_c and initial energy of E_m. The velocities of the neutron ($v_c^{'}$) after scattering and the struck atom ($V_c^{'}$) with ϕ being the scattering angle [23].

Then looking at the composite diagram relating the velocities of the two system allows for analysis on the transferred energy shown in Fig. 3.

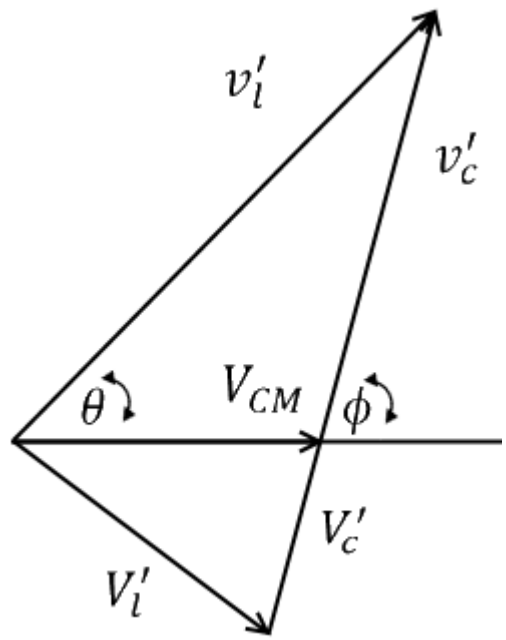

Figure 3. Elastic collision relating velocities of two systems

Combining the two vector scenarios together, it is possible to relate the recoil target nucleus velocity to ϕ. The law of cosines gives:

$$V_l^{'2} = V_{CM}^2 + V_c^{'2} - 2V_{CM}V_c^{'}cos(\phi). \tag{22}$$

Putting the velocities in terms of energy and then substituting it back into equation (22) solving for the energy transferred to the atom gives:

$$T = \frac{mM}{(m+M)^2}\,E_i + \frac{m}{M}\,E_m^{'} - 2\left(\frac{m}{m+M}\right)(E_iE_m^{'})^{1/2}\,\cos(\phi). \tag{23}$$

Now relating E_i and $E_m^{'}$, this can be simplified down even further

$$E_m^{'} = E_i\left(\frac{M}{m+M}\right)^2. \tag{24}$$

Substituing (24) into (23) gives

$$T = \frac{\gamma}{2} E_i(1 - \cos(\phi)), \tag{25}$$

$$\text{where} \qquad \gamma = \frac{4mM}{(m+M)^2}. \tag{26}$$

Equation (25) tells us that the largest value of energy transfer occurs when the particle back-scatters, and the smallest value occurs when it misses.

Now it is possible to determine the probability of a neutron interacting with the lattice by using the equations above and relating the result back to the differential scattering cross section from equation (20). Therefore, we look at the probability of the collision that scatters the neutron into a center of mass angle in the (ϕ, dΩ) range. The differential probability will be written in equivalent center of mass variables.

$$\sigma_s(E_i, \phi)\mathrm{d}\Omega = \sigma_s(E_i, T)\mathrm{d}T. \tag{27}$$

In three dimensions, dΩ can be written as the change in area over r^2. This gives :

$$\mathrm{d}\Omega = 2\pi sin(\phi)\mathrm{d}\phi. \tag{28}$$

Substituting this back into equation (27) yields:

$$\sigma_s(E_i, T)\mathrm{d}T = 2\pi\sigma_s(E_i, \phi)sin(\phi)\mathrm{d}\phi. \tag{29}$$

Taking the derivative of equation (25) and substituting it into the previous equation gives:

$$\sigma_s(E_i, T) = \frac{4\pi}{\gamma E_i}\sigma_s(E_i, \phi). \tag{30}$$

This ends up being symmetrical from $[0, \frac{\pi}{2})$ and from $(\frac{\pi}{2}, \pi]$ allowing for the total elastic scattering cross section to be rewritten as

$$\sigma_s(E_i) = 2\pi \int \sigma_s(E_i, \phi) sin(\phi) \mathrm{d}\phi. \tag{31}$$

Assuming that elastic scattering is independent of scattering angle in the center of mass system, indicating that scattering is isotropic, then:

$$\sigma_s(E_i) = 2\pi\sigma_s(E_i, \phi) \int sin(\phi)\mathrm{d}\phi = 4\pi\sigma_s(E_i, \phi). \tag{32}$$

$$\sigma_s(E_i, T) = \frac{\sigma_s(E_i)}{\gamma E_i}. \tag{33}$$

This means that the scattering cross section is independent of the transfer energy. Therefore, the probability that a neutron elastically scattering against an atom will transfer a set amount of energy is independent from the recoil energy. The average recoil energy can be calculated for a material as shown in equation (34).

$$\bar{T} = \frac{\int_{\check{T}}^{\hat{T}} T\sigma_s(E_i, T)\mathrm{d}T}{\int_{\check{T}}^{\hat{T}} \sigma_s(E_i, T)\mathrm{d}T} \approx \frac{\hat{T}}{2} = \frac{\gamma E_i}{2}, \tag{34}$$

where $\hat{T}$ and $\check{T}$ are the maximum and minimum energy transferred respectively. For a 1 MeV incident neutron we can find both γ and $\hat{T}$ as seen in Table 2.

Table 2. Semiconductor material energy values.

Material	E_i (MeV)	γ	$\hat{T}$ (MeV)
Si	1	0.133868	0.066934
Ge	1	0.0540322	0.0270161
Sn	1	0.0334172	0.0167086

III. Samples and Experiment Setup

3.1 Samples

Two sample types were used for this study. The labels that are used for identifying the samples are: Ge#64 and SnGeP 32A. These were labeled by our collaborators based on their convention. The structure, tin composition, post-growth annealing, conductivity type, doping, and thickness of the materials are listed in Table 3.

Table 3. Description of the two samples used in this study. The information was obtained from our collaborators from the Arizona State University.

Sample #	**Ge #64 wafer**	**SnGeP 32A**
Structure	bulk Ge	GeSn/n-Si (100)
Composition	0% Sn	0.9% Sn
Annealing		700 $°C/10\,s$
Type	n	n
Doping (cm^{-3})	undoped	1.5×10^{19} Phosphorous
Thickness, epilayer (nm)	0.5 mm	525

The n-Si substrate does not have a reported thickness; however, it is estimated to be around 500 μm. The pieces obtained vary in size. The pieces were cut to make sample sizes that were most ideal for the PL systems. The nominal sample size was $5 \times 5\,mm$. The Ge sample is a indirect bandgap material, while the $Ge_{0.991}Sn_{0.009}$ is a direct bandgap material due to the tin concentration and phosphorous doping.

3.2 Photoluminescence

The photoluminescence system setup can be seen in Figure 4. The system starts with an argon ion laser electrically pumped at 9.5 W at a wavelength of 514 nm. The visible laser then optically pumps into the Ti-Sapphire tunable laser, changing the wavelength to 830 nm. The laser generates an infrared beam that is focused using a $f = 4\,cm$ aspheric achromatic doublet lens with anti-reflective NIR (near-infrared)

coating. The coating minimizes the loss of power and spot size. The light next passes through a chopper to regulate the frequency of the laser pulse. This is controlled by the SR 540 Chopper Controller at 200 hertz. Aspheric lenses focus the beam to approximately 150 μm.

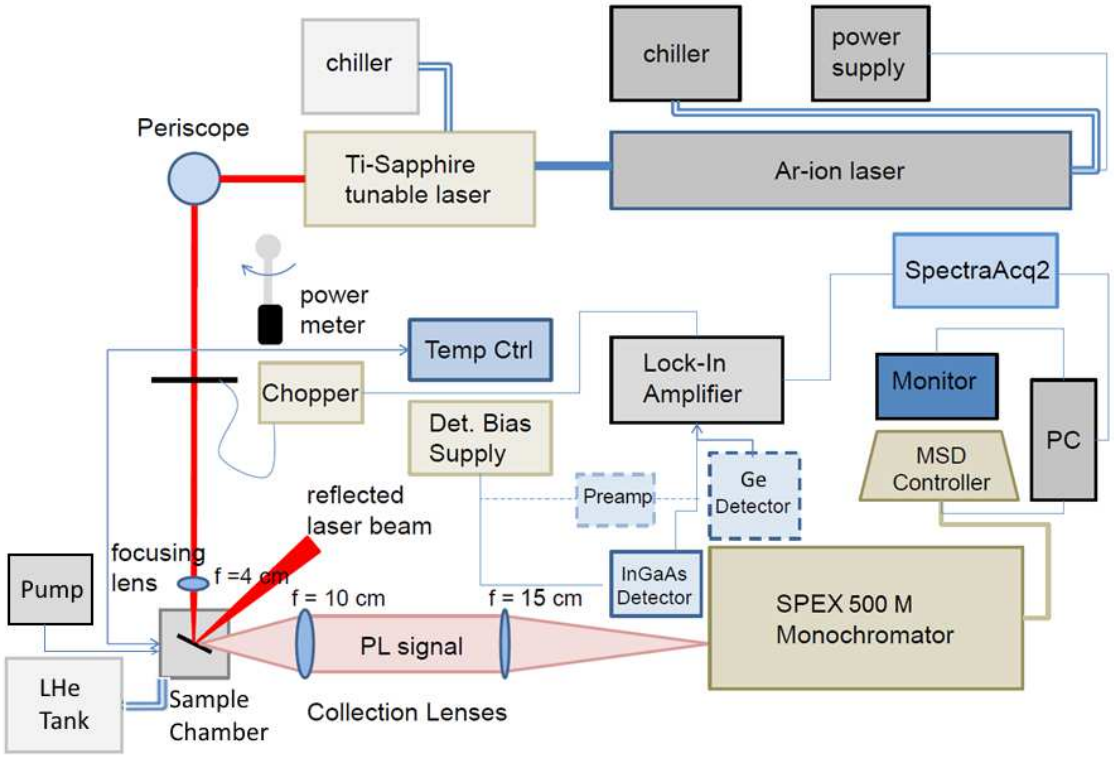

Figure 4. The photoluminescence setup which generates an IR light which hits the sample at about 45° angle to let the luminescence of the sample be measured by the monochromator and InGaAs detector.

The light then travels to the sample chamber which holds the sample at about 45° angle to the incoming laser. When doing temperature dependence, the sample chamber uses the Helitran cold finger, which is held under vacuum at 20 $mTorr$ that is verified by an attached pressure gauge. In addition, the cold finger is cooled to 3 K with helium by a Sumitomo Cryogenics F-70 system. This system is controlled with a LakeShore 331 temperature controller and is attached to a heater to moderate the temperature. The temperature is taken at two distinct points in the cold finger using silicon diodes as measurement units at the top and bottom of the apparatus.

The sample is mounted in the cold finger, which reflects or luminates the light. The luminescence from the sample passes through a purge tube, which contains two more lenses. This purge tube is filled with nitrogen gas so as to minimize atmospheric interactions on the path to the monochromator. Based on the atmosphere's composition, each element has different spectral properties and absorption wavelengths. Nitrogen is the only element in air which is not in the wavelengths that are being measured [24]. Collimating lenses, composed of CaF_2 at $f = 100\ mm$ and $f = 300\ mm$, are used in this purge area to focus the luminescence into the SPEX 500M monochromator.

A long-pass filter of 1050 nm filters the incoming light through an adjustable 1-3 mm slit into the monochromator. The monochromator has a 600 $groove/mm$ dispersion ruled diffraction grating, blazed at 1.6 μm. There are two detectors on the monochromator. The detector that is used is based on the luminescence wavelength and resolution desired. The first is the InGaAs detector which has a range of $250 - 2300\ nm$ and is mounted on the front. The second detector is the North Coast Ge detector with a range of $1000 - 1800\ nm$ with a multi-magnitude increase in resolution over the InGaAs detector, and is mounted on the side. Both detectors have adjustable slits ranging from $1 - 3\ mm$. Both are cooled with liquid nitrogen. In this study, the InGaAs was used due to increased wavelength range and satisfactory sensitivity capabilities. The output of the detectors passes through a PA-9 Transimpedence Preamplifier to a power supply and a Lock-in Amplifier. The chopper is hooked up in conjunction with the amplifier to improve signal-to-noise ratio.

3.3 Neutron Radiation

The samples were taken to the Ohio State University Nuclear Reactor Lab for irradiation in their neutron reactor. There are multiple beam ports and dry tubes as irradiation facilities in the pool-type reactor. The reactor is licensed for a maximum of

500 kW thermal power. This has a maximum thermal flux in the central irradiation facility of 1.4×10^{13} $n/cm^2/s$.

The samples were placed inside a 7-inch tube that was directly outside of the reactor. The samples were put inside a cadmium box with the top of the sample facing the core. The cadmium box absorbs neutrons with a very high probability ($\approx 97\%$) if the neutron energy is below the cadmium cut-off of 0.5 eV. This leaves an equivalent neutron flux of 1 MeV to irradiate the samples. While the reactor was being raised to full power, the samples were out of the tube so that no additional reaction occurred that was not measured. Once the reactor was at full operating power for the experiments at 450 kW, the samples were placed into the tube 20 ft down, in the depth of the core. The samples received a 1 MeV equivalent flux of 2.0×10^{11} $\frac{n}{cm^2 s}$. They were each irradiated for 3.5 hours at a neutron energy equivalency of 1 MeV. This means there was a total neutron flux of 2.52×10^{15} $\frac{n}{cm^2}$.

3.4 Annealing

The above room temperature annealing process was performed using a Thermo Scientific Lindberg Blue M tube furnace. The samples were held on a glass rod with a paddle end at the center of the tube furnace which was held at a constant 60° C. The samples were annealed at the center for thirty minutes each time, except the first instance where it was annealed for ten minutes. The time was recorded externally on a stopwatch. All other annealing was performed at room temperature.

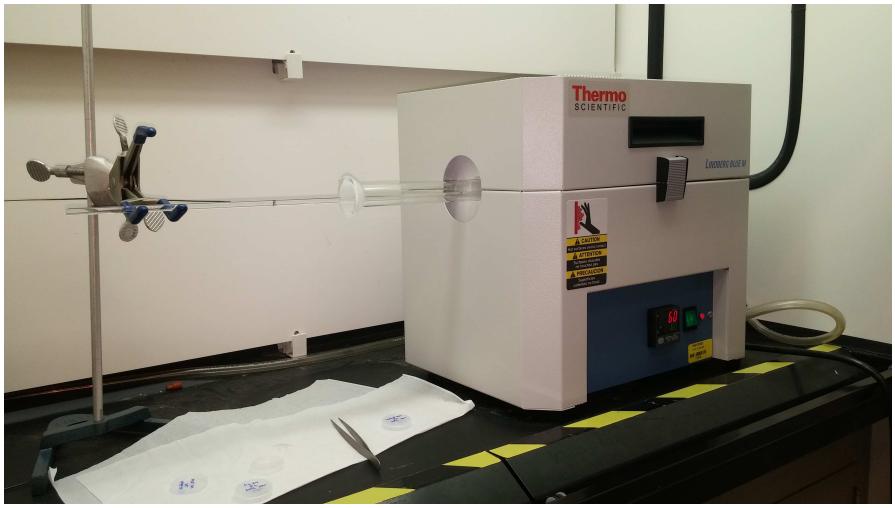

Figure 5. Annealing tube furnace that was set to $60\ ^{\circ}C$

IV. Results and Analysis

4.1 Pre-Characterization

Neutron irradiation displaces some atoms from the lattice. The atoms removed from the local lattice are new created vacancies in the lattice structure. The surrounding atoms move further away from the location of the displaced atom due to the stronger pull of the nearest neighbors versus the pull from the vacancy or displaced atom. The displaced atoms remain bonded to the surrounding atoms. Because the neutron radiation causes large amounts of lattice displacement and some vacancies, defect clusters may form [25–28]. These defect clusters may change the energy band and localized electron density distribution. They also cause the bandgap related PL intensity to decrease with increasing displacement and vacancy concentrations. The PL measurements made one week after the neutron radiation of total flux $2.52 \times 10^{15}\ \frac{n}{cm^2}$ definitively show the bandgap transition PL degradation, as seen in Fig. 6.

The neutron radiation damage is not fully permanent. While there may be permanent damage done to the samples, the annealing methods of both room temperature and 60 $°C$ annealing allow for recovery of the damaged samples' properties.

4.2 Ge Wafer

The germanium wafer is the bedrock of these experiments. As understanding of the foundation semiconductor material grows, it is able to be translated over to closely related alloys. Germanium is a strong indirect bandgap material. After putting the sample in 1 MeV equivalent neutron radiation for 3.5 hours at a flux rate of $2.0 \times 10^{11}\ \frac{n}{cm^2 s}$, the neutron damage was very significant. The neutron radiation caused a large amount of displacement and some vacancies in the material. As is seen

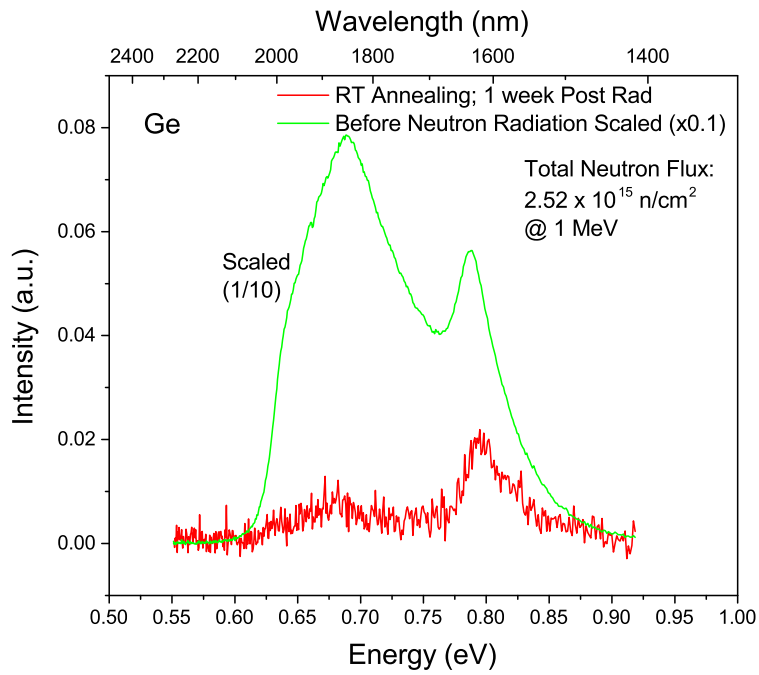

(a) Ge

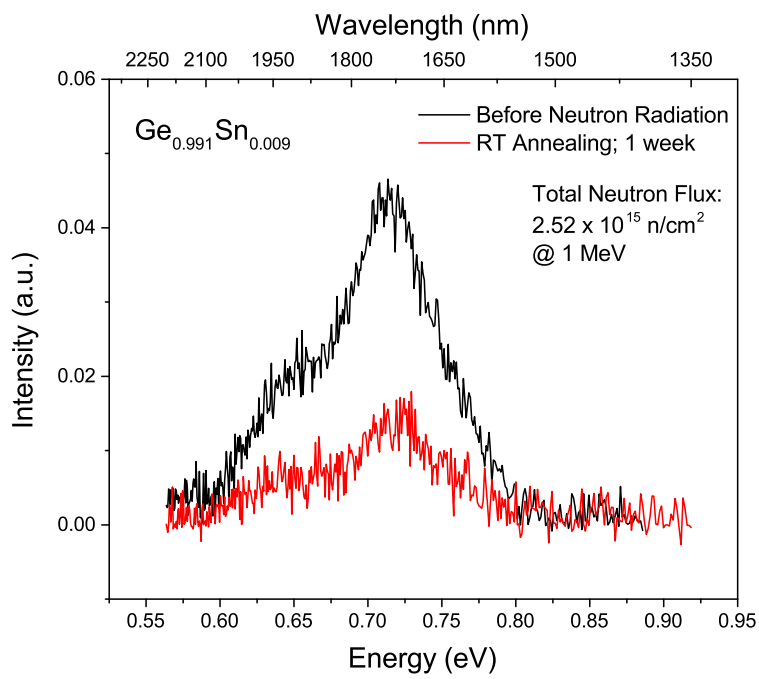

(b) $Ge_{0.991}Sn_{0.009}$

Figure 6. PL representation of neutron radiation damage to each of the samples. In each figure the PL before radiation (black) is compared to the PL one week after neutron radiation (red).

in Fig. 7, the original PL signal is no longer distinguishable.

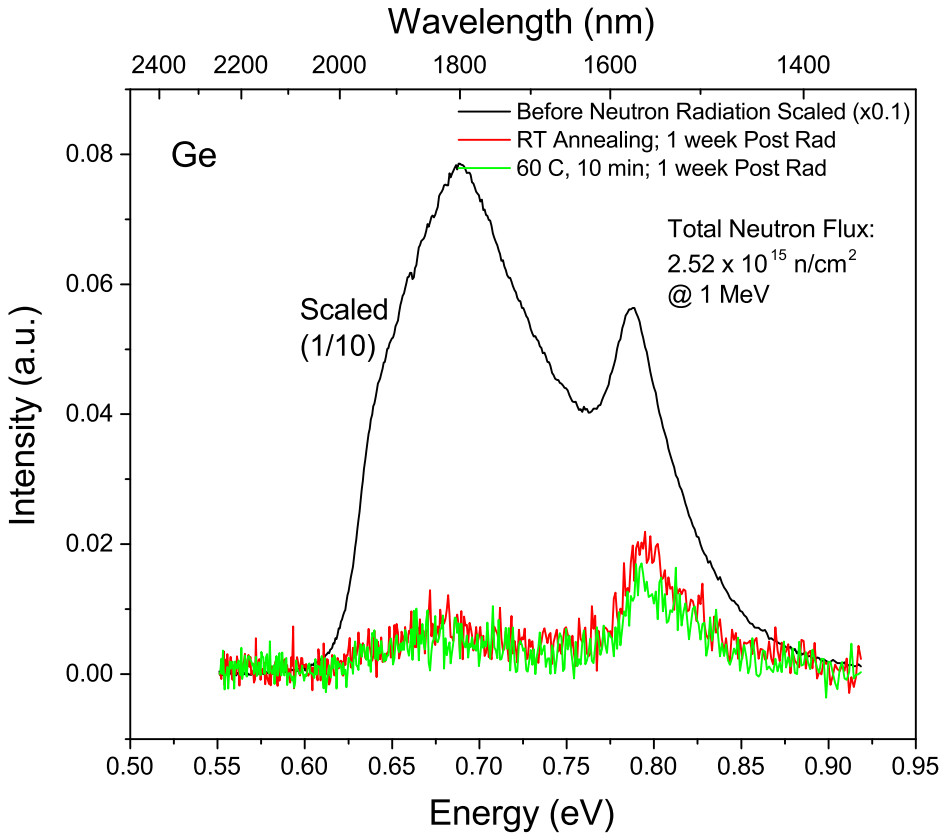

Figure 7. Comparison of the germanium sample after neutron radiation versus before radiation. The indirect bandgap peak is at $0.68\ eV$ and the direct bandgap peak is at $0.78\ eV$. After neutron irradiation, the direct and indirect bandgap intensities greatly decreased to 4% and 1%, respectively. Two samples were irradiated. Both samples were annealed for one week at room temperature. The second sample had an additional 10 minutes of annealing at $60\ °C$.

The neutron radiation dramatically changed the material properties of the semiconductor material. The PL degradation shows that the bandgap PL intensity was greatly altered from the neutron irradiation. During the annealing process, the displaced atoms are slowly repositioned back to the correct lattice configuration. As this occurs, the gradual damage recovery also increases the intensity of the PL signal. This can be seen over the span of four weeks of annealing, as shown in Fig. 8 on page 29, where the increase of PL intensity in both the indirect and the direct

bandgap-related transitions is evident. This figure shows both the room temperature annealed sample (Fig. 8a) and the 60 $°C$ annealed sample (Fig. 8b). The 60 $°C$ annealed sample received a week of room temperature annealing, then annealed at 60 $°C$ for a total time of 10, 40, 70, and 100 minutes. That is, for the fourth week it was annealed for an additional thirty minutes from the third week.

The growth of PL intensities after RT and 60 $°C$ annealing is evident in Fig 8. Significant improvement is observed after the first week of post neutron radiation, with the increase of the indirect bandgap intensity, from 1% of the pre-neutron irradiation to 3% for both samples. The increase of the direct bandgap intensity is also seen from the 4% of the pre-neutron irradiation to 7% for the room temperature annealed sample and 11% for the 60 $°C$ annealed sample. It is also important to note that the direct bandgap radiative transition is returning more quickly, which is currently working on the sample to make a better direct bandgap material.

Because annealing in general is working to return the sample to its original state, it is also necessary to compare 60 $°C$ and room-temperature annealing in order to determine which is more effective. It appeared that the use of 60 $°C$ annealing did not aid in the recovery of the PL signal for the germanium sample at the beginning. For the first three weeks post-neutron radiation, the recovery of PL intensity is almost identical, as can be seen in Fig. 9 on page 30. That is, the difference between the PL signals for RT and 60 $°C$ annealing is negligible. However, when looking at week four, there is a sizable difference between the two PL signals. This means that the 60 $°C$ annealing does make a difference after a long enough period of time. This effect can be seen in Fig. 9 (page 30) and/or Fig. 10 (page 32).

The max PL intensity value obtained after room temperature annealing is 0.041 at 0.795 eV for the direct bandgap transition, while that for the 60 $°C$ annealed sample is 0.062 at 0.789 eV. This means that the max PL peak value for the 60 $°C$ annealed

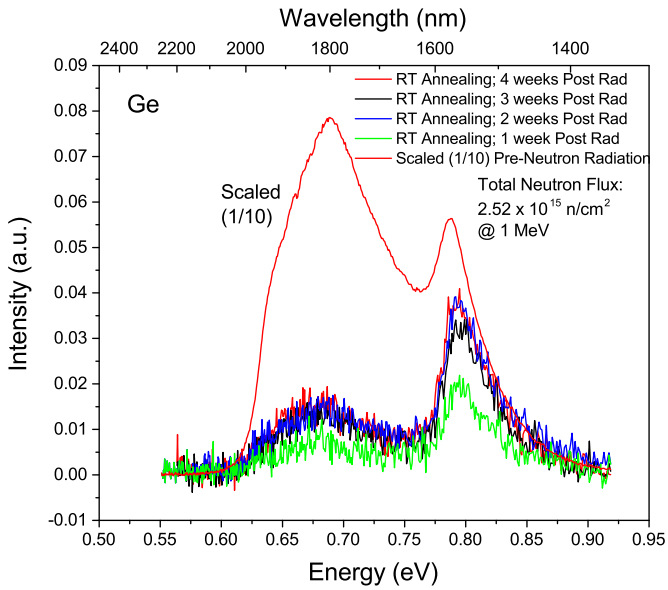

(a) PL measurements after room temperature annealed sample over four weeks

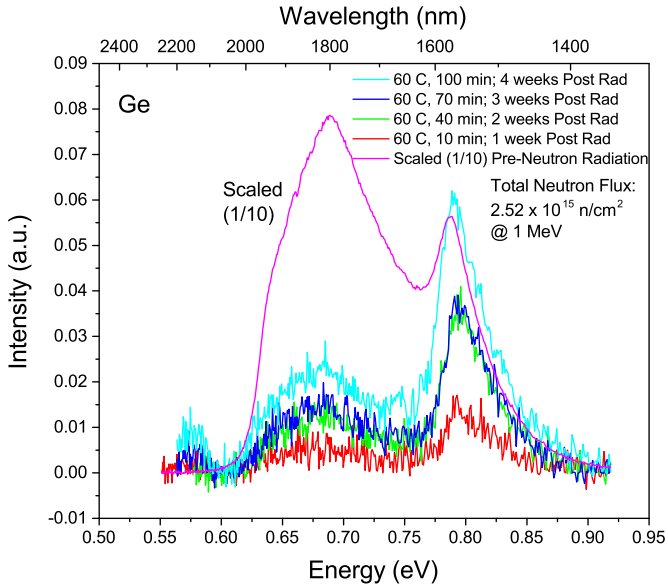

(b) PL measurements after 60 $°C$ annealed sample over four weeks

Figure 8. Ge bandgap PL growth over four weeks after neutron radiation. This shows that there is recovery of the direct bandgap PL at $\sim 0.8\ eV$. The indirect bandgap PL is recovering much slower at $\sim 0.68\ eV$. The RT sample (Fig. 8a) recovered 7% of its direct bandgap intensity and 3% of its indirect bandgap intensity of the pre-irradiated PL intensity after four weeks from radiation. The $60\ °C$ annealed sample (Fig. 8b) recovered 11% of its direct bandgap intensity and 3% of its indirect bandgap intensity of the pre-irradiated PL intensity after four weeks from radiation and 100 minutes accumulated $60\ °C$ annealing.

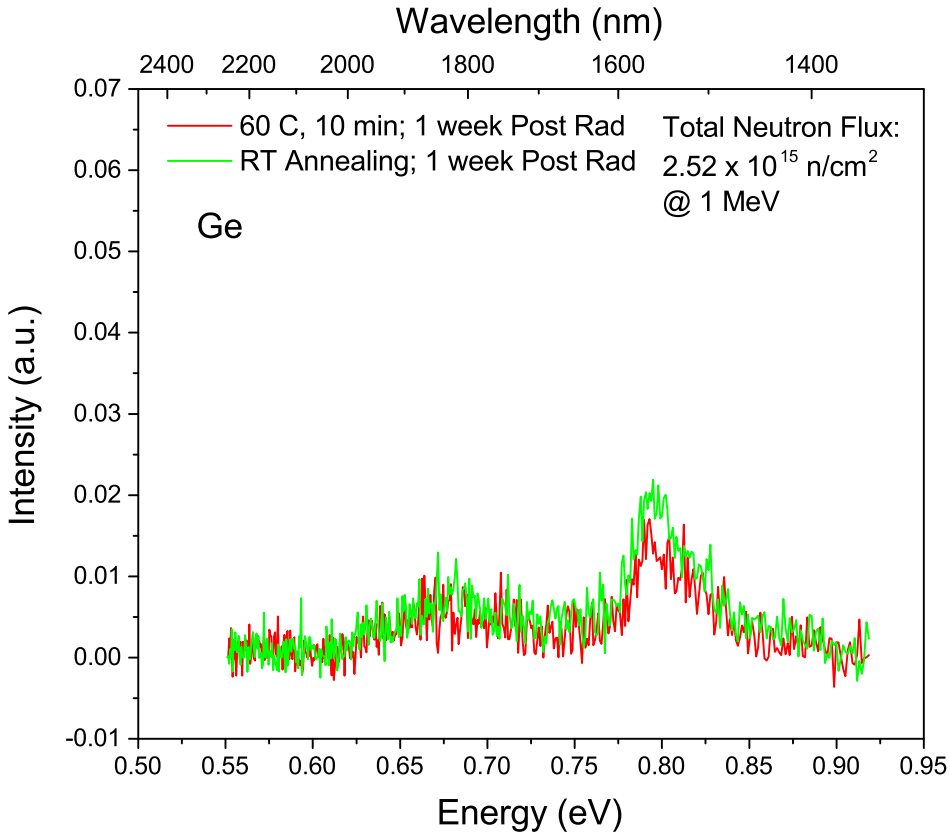

(a) PL measurements after one week post irradiation

Figure 9. PL comparison between room temperature annealed and the $60\ ^{\circ}C$ **annealed post neutron irradiated Ge sample. In figure 9a, the samples are compared after one week of room temperature annealing, and the second sample with an additional 10 minutes of** $60\ ^{\circ}C$ **annealing. The maximum separation of the PL signal is 22% greater for the RT annealed sample versus the** $60\ ^{\circ}C$ **annealed sample. In figure 9b, the samples are compared after two weeks of room temperature annealing, and the second sample with 40 total minutes of** $60\ ^{\circ}C$ **annealing. The maximum separation of the PL intensities being 5% greater for the RT annealed sample versus the** $60\ ^{\circ}C$ **annealed sample. In figure 9c, the samples are compared after three weeks of room temperature annealing, and the second sample with 70 total minutes of** $60\ ^{\circ}C$ **annealing. The maximum separation of the intensities being 14% greater for the the** $60\ ^{\circ}C$ **annealed sample versus RT annealed sample.**

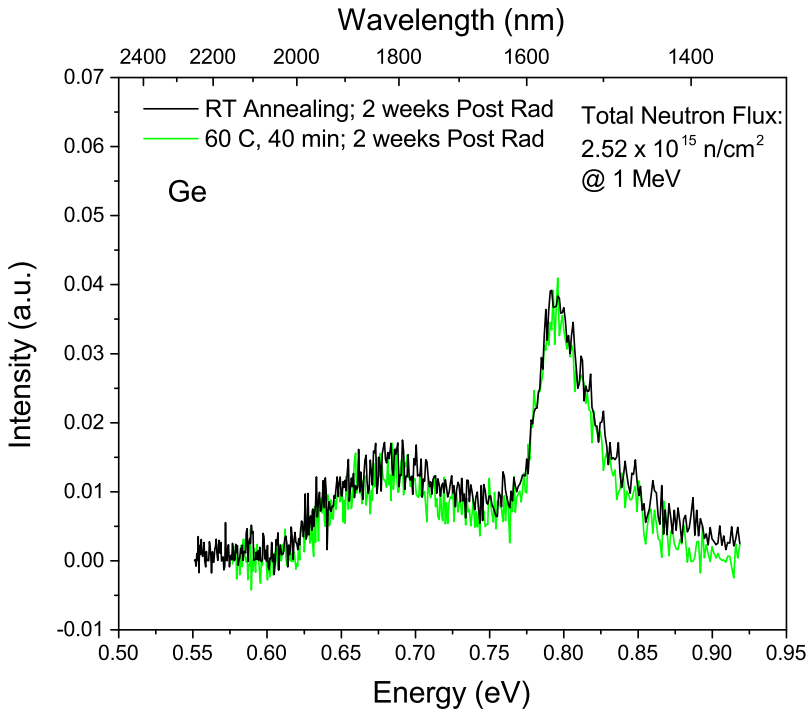

(b) PL measurements after two weeks post irradiation

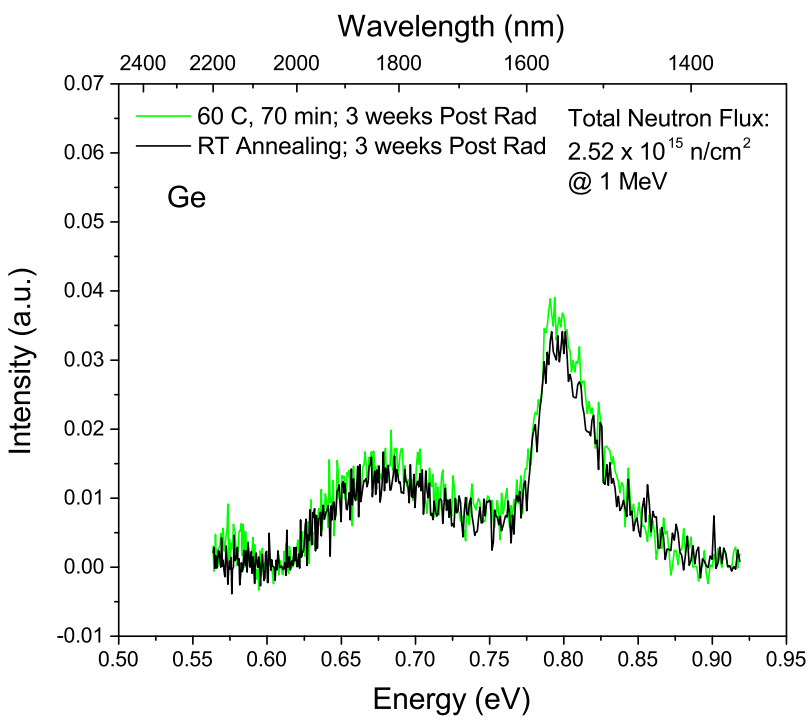

(c) PL measurements after three weeks post irradiation

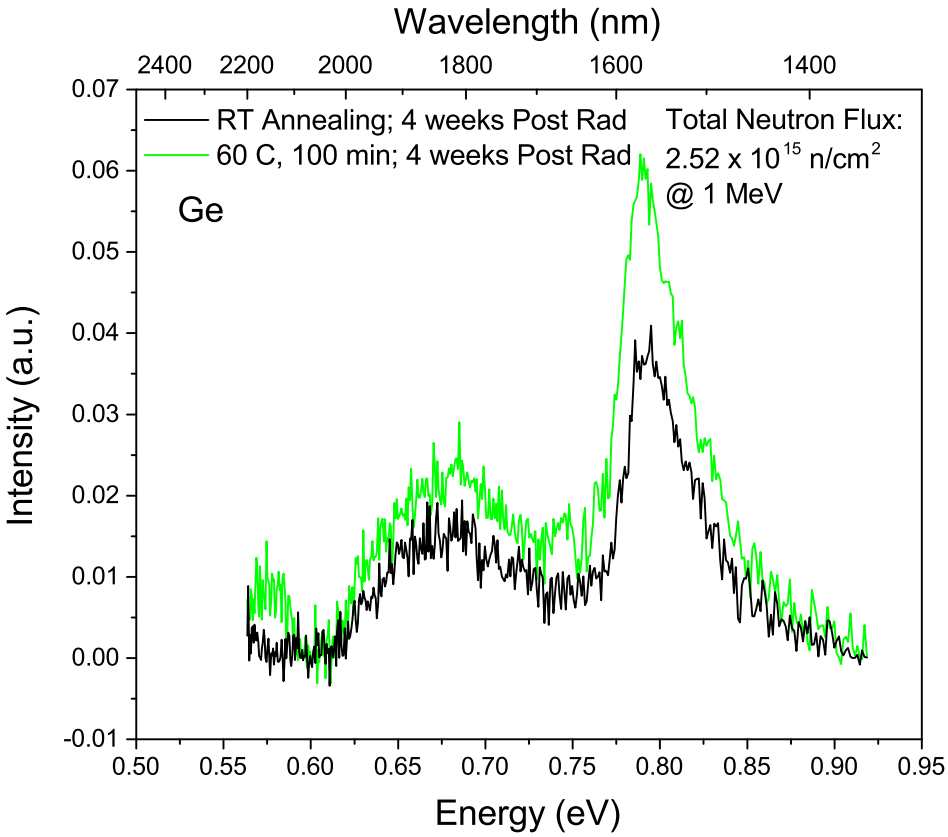

Figure 10. Comparison of the germanium sample after neutron radiation. The first PL is the room temperature annealed sample after four weeks. The second is the annealed sample after four weeks of room temperature annealing and a total of 100 minutes of annealing at $60\ ^{\circ}C$. The $60\ ^{\circ}C$ annealed PL signal has a maximum separation of 52% greater then the RT PL signal, which is at the direct bandgap peak.

sample is 51.6% greater than that for the room temperature annealed sample. For the indirect bandgap-related PL, the room temperature annealed sample had a max PL peak of 0.019 at 0.687 eV, while the 60 °C annealed sample had a max PL peak value of 0.029 at 0.685 eV. That is, the max PL peak intensity for the indirect bandgap transition is 49.5% higher than that for the room temperature annealed sample. Therefore, for the germanium sample, it is evident that the 60 °C annealing is important for increasing the efficiency of the sample recovery. Doing a linear extrapolation allows us to show a very rough estimation of how long annealing will take to recover the original PL intensity after irradiation. From this extrapolation, the 60 °C annealed sample will take less then half the time compared to the room temperature annealed sample, as is seen in Fig. 11 and table 4.

Table 4. Extrapolation values approximating the length of time needed to fully recover the original direct and indirect bandgap PL intensity of Ge. Calculations are based on the direct and indirect bandgap PL intensities before neutron irradiation. r^2 indicates how well the data fits to a linear model, with a perfect fit being 1.

	Time	r^2	Difference
60°C Anneal Direct Bandgap PL	26 weeks	0.898	54 weeks
RT Anneal Direct Bandgap PL	80 weeks	0.5209	
60°C Anneal Indirect Bandgap PL	86 weeks	0.965	81 weeks
RT Anneal Indirect Bandgap PL	167 weeks	0.8412	

This extrapolation provides damage recovery rate. The coefficient of determination, r^2, is a number that indicates how well the data fits the model, in this case a linear model. The values range from 0 to 1, where the closer to 1 the better the fit. There is most likely permanent damage that will not allow the full recovery of the PL intensity or complete recovery of the crystal with RT or 60 °C annealing. It is likely that higher-temperature annealing for an appropriate length of time may be needed for the full recovery of the pre-neutron radiation PL signal. The length of time for

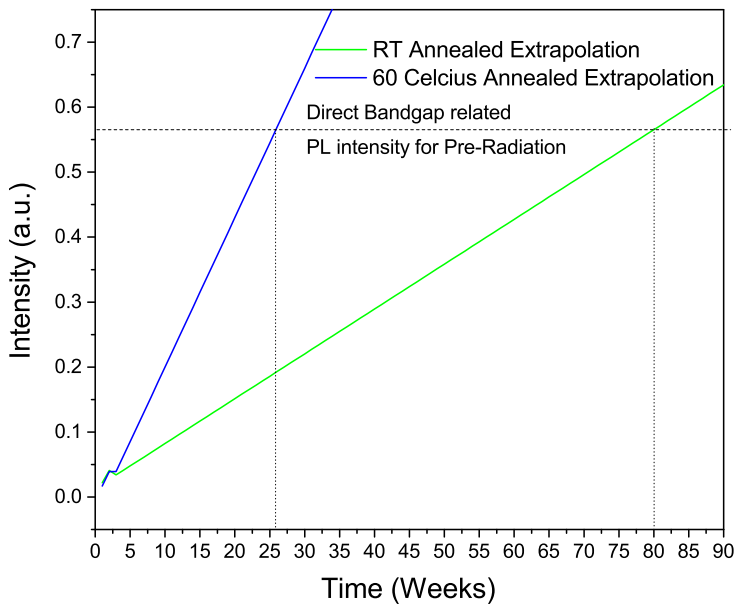

(a) Direct bandgap PL recovery extrapolation

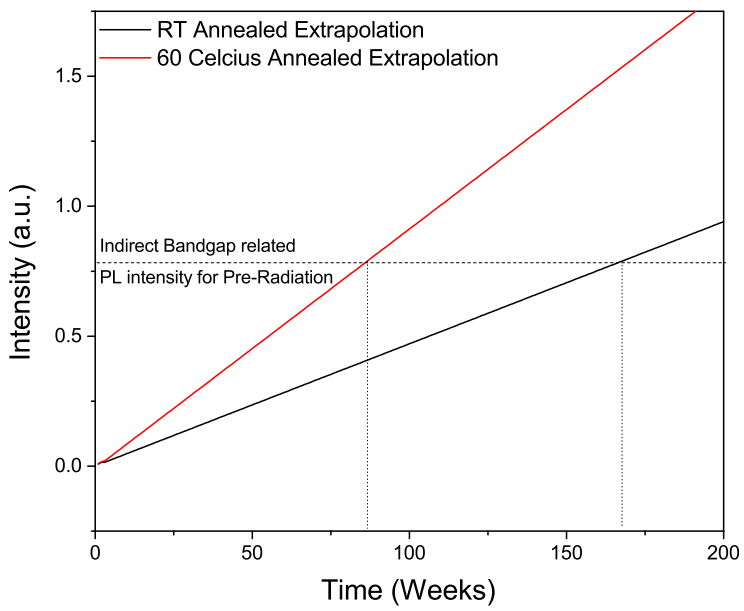

(b) Indirect bandgap PL recovery extrapolation

Figure 11. Extrapolation for rough approximate length of time needed to fully recover the original direct and indirect bandgap PL intensity of Ge. Calculations are based on the direct and indirect bandgap PL intensities before neutron irradiation.

full recovery of the PL intensity can be visualized by looking at Fig. 12. This figure shows the pre-neutron radiation PL signal along with the PL for the 60 $°C$ annealed sample over the four weeks of annealing.

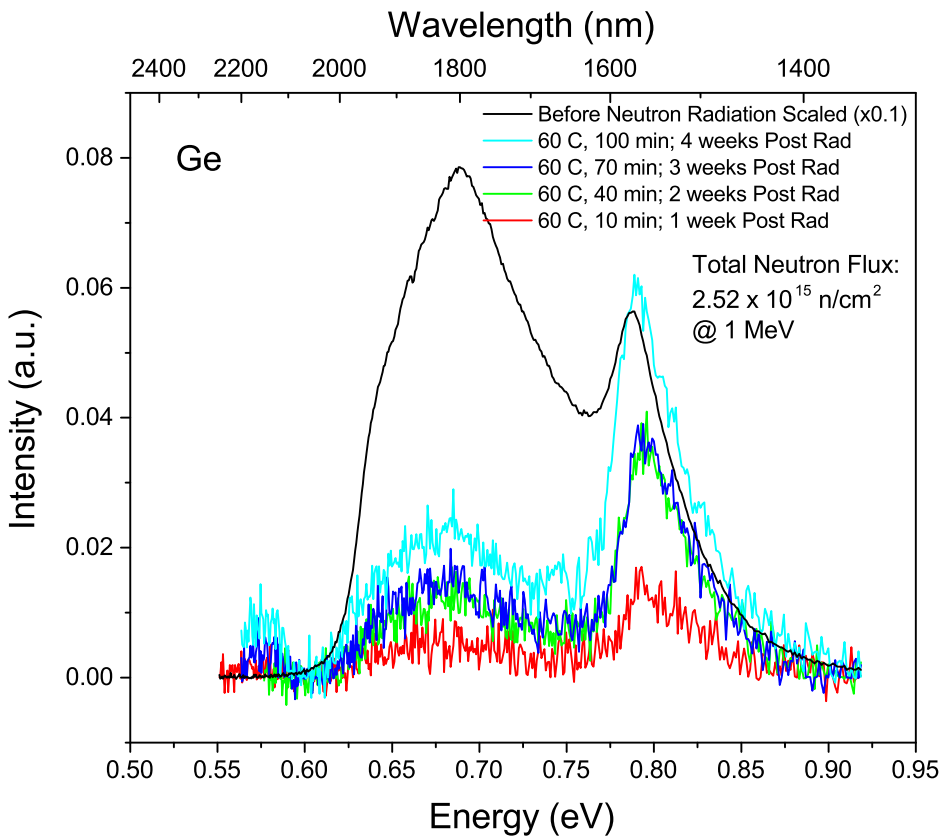

Figure 12. Comparison of PL intensities for the germanium sample after neutron radiation versus before neutron radiation. The annealed sample received 10 minutes of $60°\,C$ annealing after one week of room temperature annealing. The following four weeks received an additional 30 minutes of $60°\,C$ annealing after each week passed. The total $60\,°C$ annealing time, after four weeks, is 100 minutes of $60\,°C$ annealing.

4.3 $Ge_{0.991}Sn_{0.009}$

The $Ge_{0.991}Sn_{0.009}$ sample is an n-type material doped with phosphorous on a silicon substrate. The phosphorous doping adds extra electrons to the material. This means a higher carrier concentration is present due to the heavy doping. The thin

layer of GeSn with high doping will create closer to direct bandgap material behavior. The tin concentration shifts the effective bandgaps, making the indirect bandgap overlap the direct.

The neutron radiation displaced a large amount of atoms and created new vacancies in the material. Additional interactions will occur between the GeSn and the silicon substrate. A defect layer may form between the GeSn that is adhered on the silicon substrate due to the different length lattices, making vacancies more difficult to repair. The displacements and vacancies created in the material will cause a decrease in the number of available electrons, by creating additional bonding sites and holes in the material. This will directly correlate to a decrease in the PL intensity due to the increase of disorder in the material.

The effects of the neutron radiation on the PL signal can be seen in Fig. 13. This figure shows the comparison between the PL signal before neutron radiation and after one week of annealing. Two independent samples cut out of one Ge wafer were used for this experiment. The first received only room temperature annealing (or kept at room temperature) throughout all five weeks. The second sample received additional 60 $°C$ annealing at the end of each week. Throughout the rest of the week, it received room temperature annealing in the same environment as the other sample. The first week's measurement received an additional 10 minutes of 60 $°C$ annealing. The neutron irradiation caused the PL intensity to drop to 37% of the pre-neutron irradiation PL intensity.

After another week has passed, there was a significant improvement in the intensity of the PL signal for both the room temperature and 60 $°C$ annealed samples, as can be seen in Fig. 14 on page 38. The recovery time is much faster than the germanium sample analyzed in section 4.2. There is no discernible difference between the room temperature and the 60 $°C$ annealed samples. Both samples recovered to 67% of the

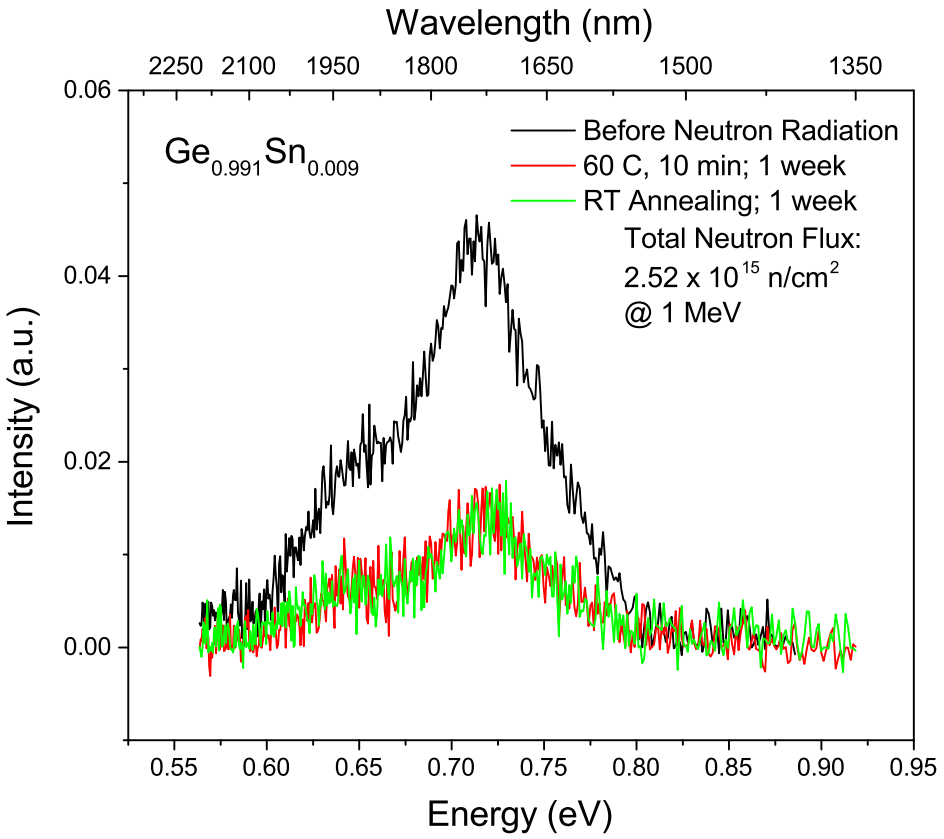

Figure 13. PL comparison of $Ge_{0.991}Sn_{0.009}$ before and after neutron irradiation. Both samples were annealed for one week at room temperature. The PL measurement of the second sample had an additional 10 minutes of annealing at $60\ ^{\circ}C$. The neutron damage reduced the PL intensity to 37% for both samples.

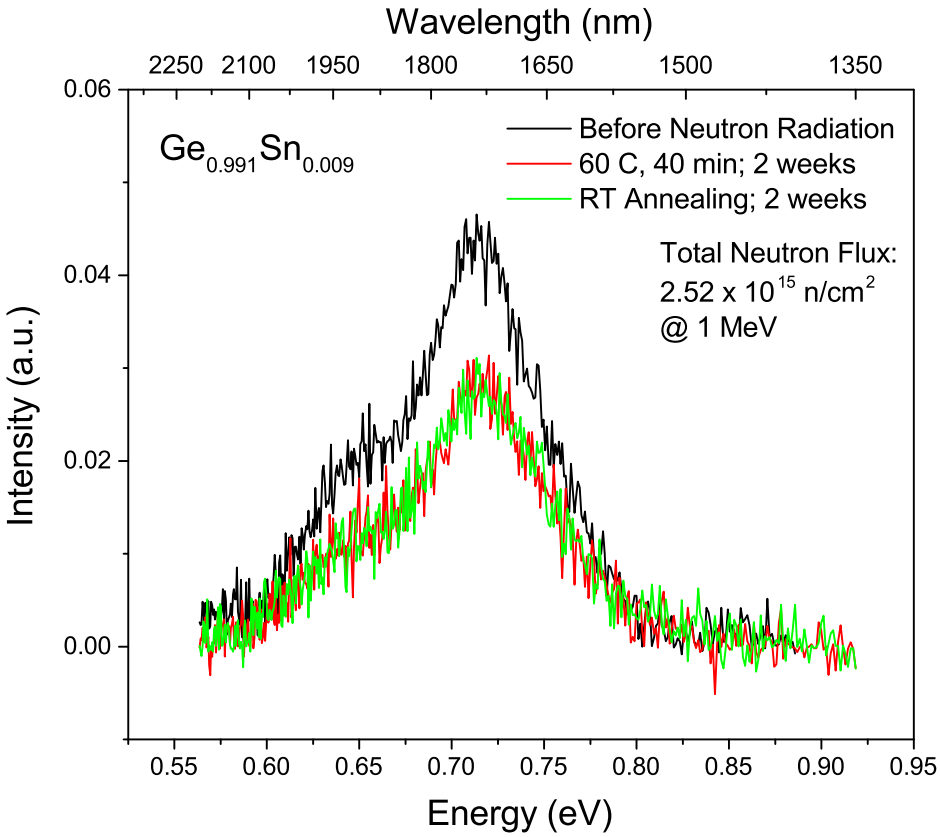

Figure 14. PL comparison for $Ge_{0.991}Sn_{0.009}$ two weeks after neutron irradiation versus before neutron irradiation. The figure shows the progress over the two weeks for the room temperature annealed sample and the $60\ ^{\circ}C$ annealed sample broken up by each week progress. Both samples were annealed for two weeks at room temperature. The second sample had an additional 10 minutes of annealing at $60\ ^{\circ}C$ after the first week. Then an additional 30 minutes of $60\ ^{\circ}C$ annealing after the second week. The samples recovered 67% of the pre-neutron irradiated intensity.

original PL intensity before neutron irradiation.

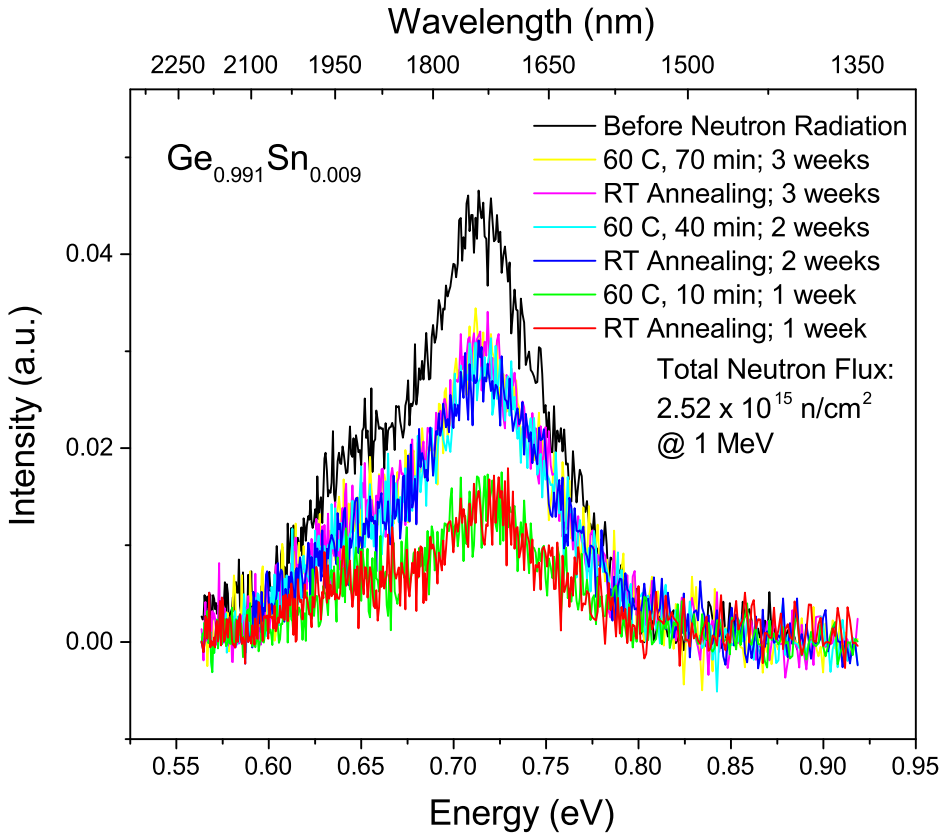

Figure 15. PL comparison for $Ge_{0.991}Sn_{0.009}$ three weeks after neutron radiation versus before neutron radiation. The figure shows the progress over the three weeks for the room temperature annealed sample and the $60\ ^{\circ}C$ annealed sample broken up by each weeks progress. Both samples were annealed for three weeks at room temperature. The PL measurement of the second sample had an additional 10 minutes of annealing at $60\ ^{\circ}C$ after the first week. Then an additional 30 minutes of $60\ ^{\circ}C$ annealing after the second and third week. There is negligible improvement between weeks two and three.

The annealing reaches a standstill for two weeks following the end of week two. This can be seen in Figs. 15 and 16. There is barely any improvement over this time period.

Additional annealing of the sample occurs after five weeks. There is a noticeable improvement, which makes almost full recovery of the sample. The PL intensity, after four weeks, improves to 88% and 86% of the pre-neutron radiation PL intensity for

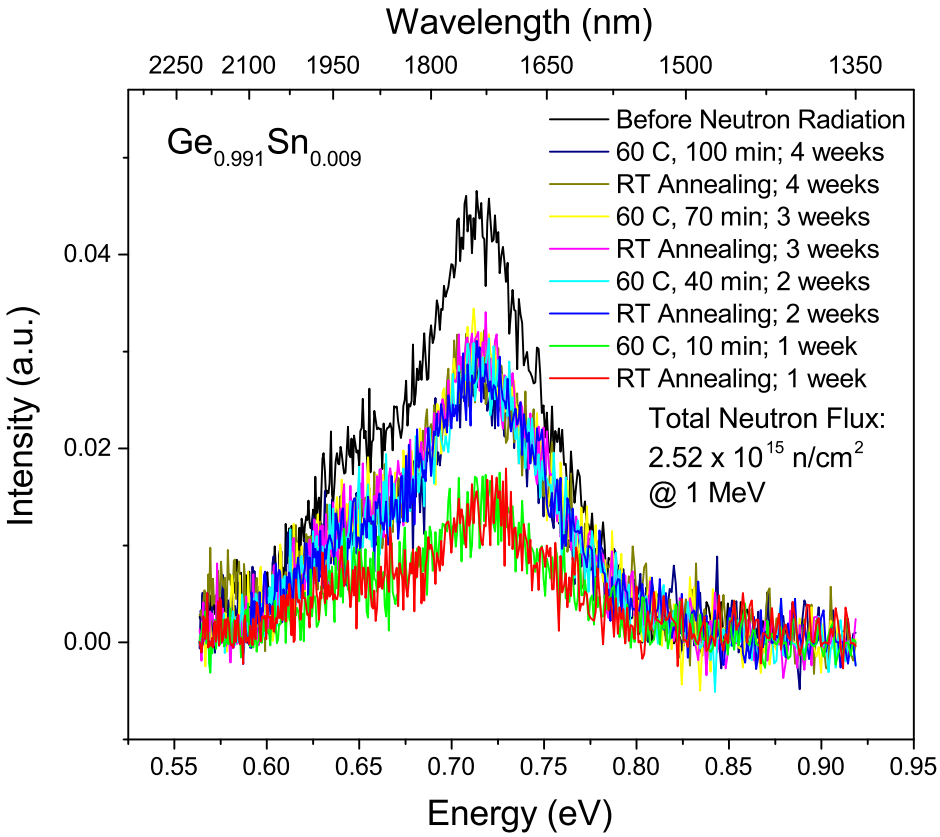

Figure 16. PL comparison for $Ge_{0.991}Sn_{0.009}$ four weeks after neutron radiation versus before neutron irradiation. The figure shows the progress over the four weeks for the room temperature annealed sample and the $60\ ^{\circ}C$ annealed sample broken up by each weeks progress. Both samples were annealed for four weeks at room temperature. The PL measurement of the second sample had an additional 10 minutes of annealing at $60\ ^{\circ}C$ after the first week. Then an additional 30 minutes of $60\ ^{\circ}C$ annealing after the second, third, and fourth week. There is negligible improvement between weeks two, three, and four.

the room temperature and 60 $°C$ annealed samples, respectively. The PL intensity increase can be seen in Fig. 17.

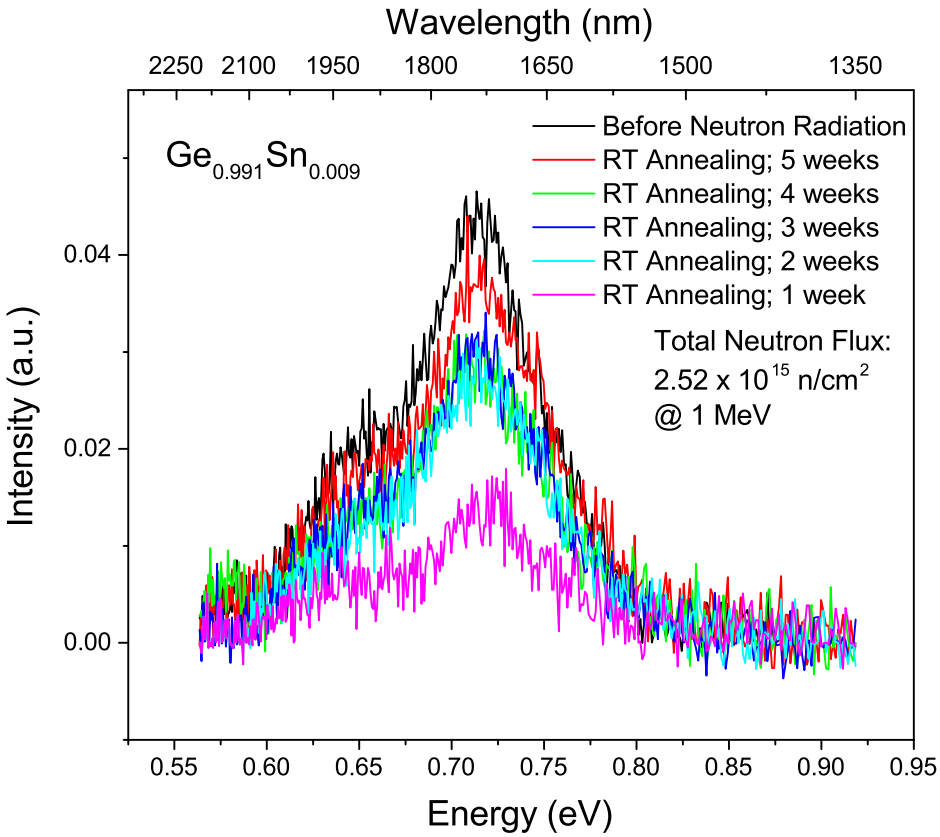

(a) PL measurements after room temperature annealed sample over five weeks

Figure 17. PL comparison for $Ge_{0.991}Sn_{0.009}$ five weeks after neutron radiation versus before neutron irradiation. The figure shows the progress over the five weeks for the room temperature annealed sample and the 60 $°C$ annealed sample broken up by each weeks progress. Both samples were annealed for four weeks at room temperature. The PL measurement of the second sample had an additional 10 minutes of annealing at 60 $°C$ after the first week. Then an additional 30 minutes of 60 $°C$ annealing after the second, third, fourth, and fifth week. There is an improvement after the fifth week. Weeks two through four recovered 67% with the fifth week recovering 88% and 86% for the RT (Fig. 17a) and 60 $°C$ (Fig. 17b) annealing respectively.

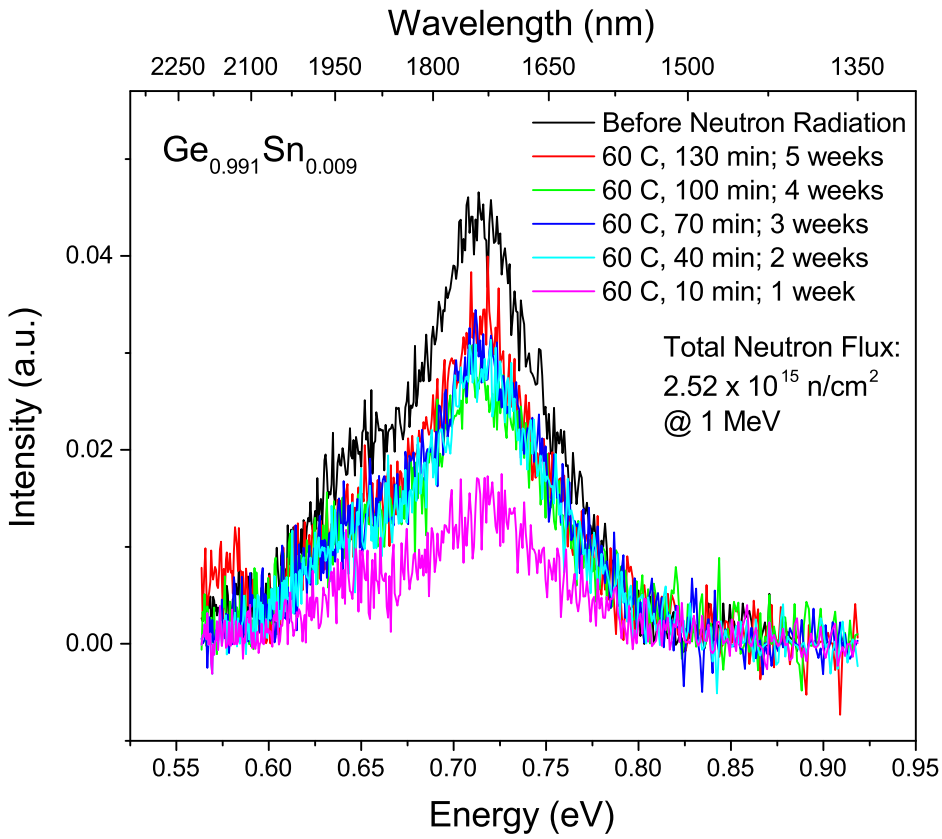

(b) PL measurements after 60 °C annealed sample over five weeks

In the first four weeks after neutron radiation, there was little to no difference in the PL intensity recovery between the room temperature annealing and the 60 °C annealing. At 5 weeks after neutron radiation, the room temperature annealing improved to 88% and the 60 °C annealing improved to 86%. The minimal difference between the annealing methods indicates that only room temperature annealing is needed for the recovery of this sample. It is possible that a higher temperature annealing or longer annealing at 60 °C or greater might decrease the recovery time. This can be examined more closely in Fig. 18.

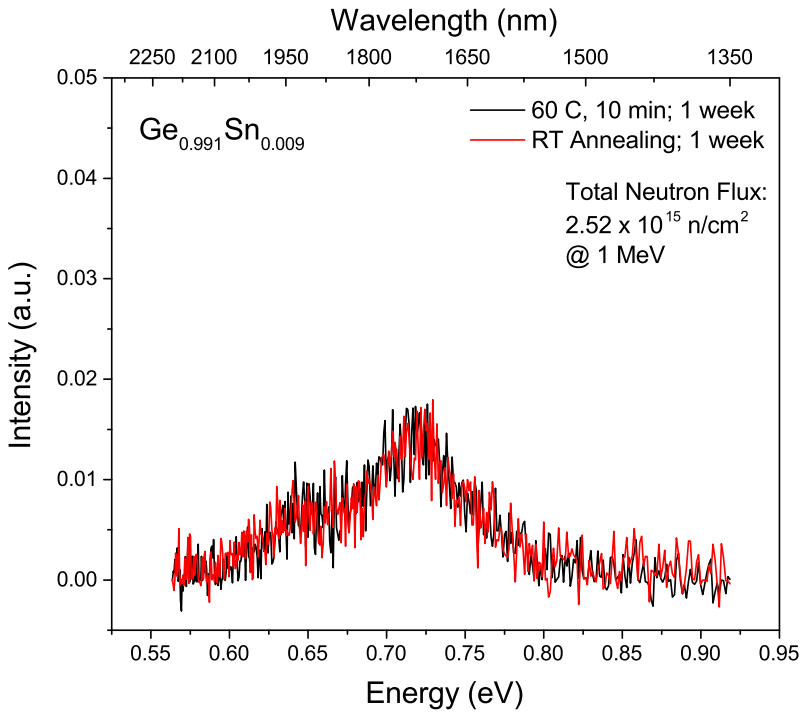

(a) PL measurements after one week post irradiation

Figure 18. PL comparison for $Ge_{0.991}Sn_{0.009}$ post neutron irradiation between room temperature annealed sample and the $60\ ^{\circ}C$ annealed sample. This shows the comparison of each passing week. Only week five shows any difference which is still minimal. Fig. 18a shows the PL measurement after one week post neutron irradiation. Fig. 18b shows the PL measurement after two weeks post neutron irradiation. Fig. 18c shows the PL measurement after three weeks post neutron irradiation. Fig. 18d shows the PL measurement after four weeks post neutron irradiation. A difference between the annealing process is seen after five weeks post neutron irradiation as seen in Fig. 18e.

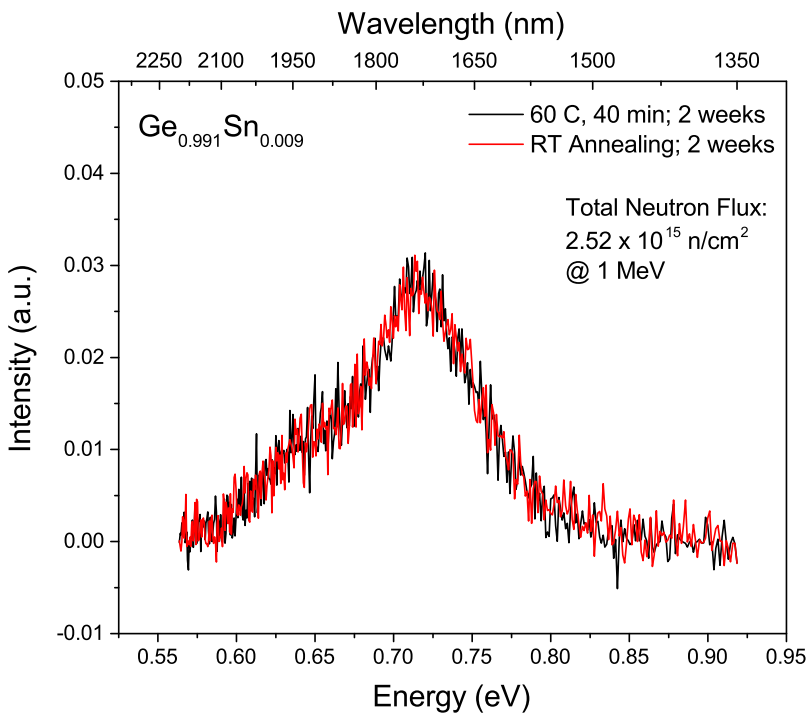

(b) PL measurements after two weeks post irradiation

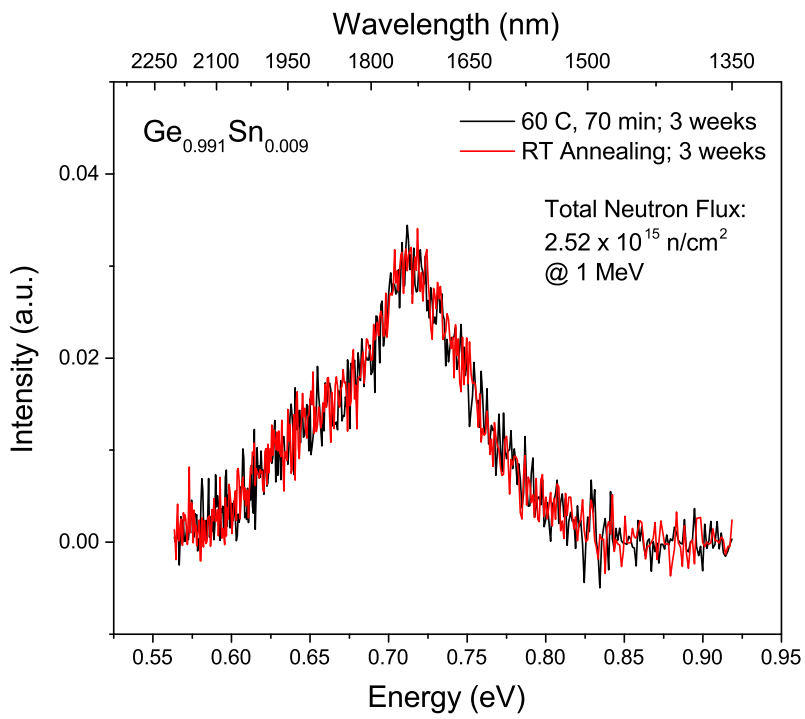

(c) PL measurements after three weeks post irradiation

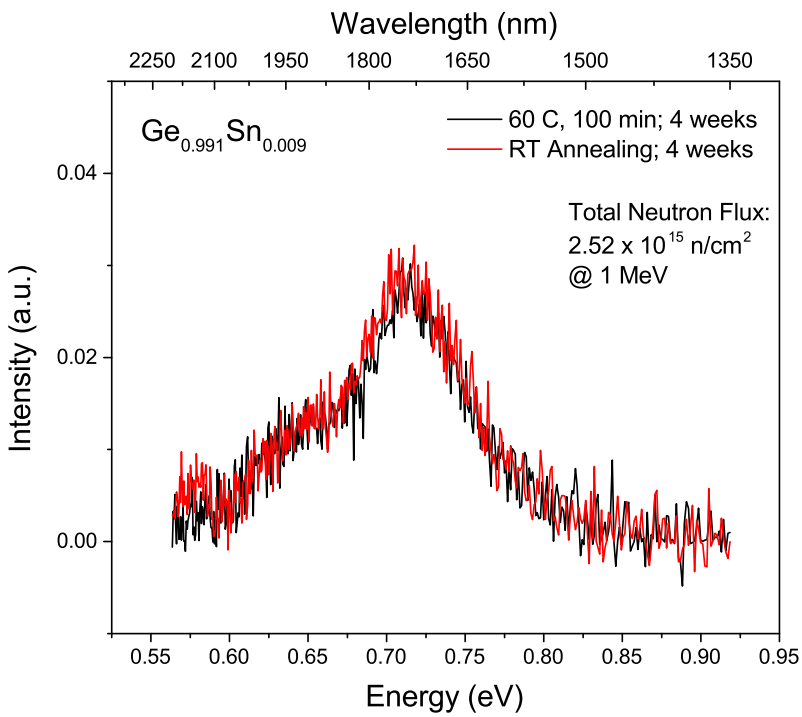

(d) PL measurements after four weeks post irradiation

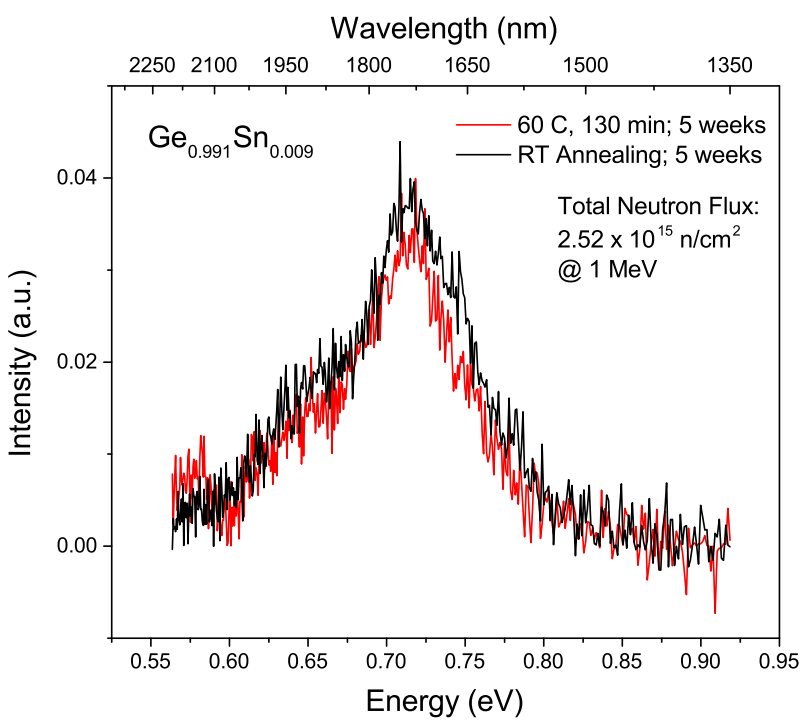

(e) PL measurements after five weeks post irradiation

In Fig. 18a, the PL intensities of the samples are compared for the first sample after one week of room temperature annealing with the second sample undergone an additional 10 minutes of 60 $°C$ annealing. In Fig. 18b, the PL intensities of the samples are compared for the first sample after two weeks of room temperature annealing with the second sample undergone 40 total minutes of 60 $°C$ annealing. In Fig. 18c, the PL intensities of the samples are compared after the first sample received three weeks of room temperature annealing, and the second sample received 70 total minutes of 60 $°C$ annealing. In Fig. 18d, the PL intensities of the samples are compared after the first sample received four weeks of room temperature annealing, and the second sample received 100 total minutes of 60 $°C$ annealing. In Fig. 18e, the PL intensities of the samples are compared after the first sample received five weeks of room temperature annealing, and the second sample received 130 total minutes of 60 $°C$ annealing.

Looking at the differences between the maximum PL peaks for each week after neutron irradiation allows for confirmation that there is not a significant enough difference to find a benefit in the 60 $°C$ annealing compared to the room temperature annealing. The first week after neutron irradiation there was a $3 \pm 2\%$ difference. The second week had a percent difference of $1 \pm 1\%$. The third week had a percent difference of $< 1\%$. The fourth week had $2 \pm 1\%$ difference and finally the fifth week had $11 \pm 7\%$ difference. These are the statistical differences of the smoothed out data.

V. Future Work

There are many different directions that can be taken from this point to further the work started in this study. Looking at alternate types of radiation will give a better understanding of the samples. Analyzing the effects on alternate tin concentrations will further the knowledge of the materials and further optimize the best new semiconductor material. Performing PL to take in situ measurements while having the sample under constant higher the room temperature annealing would bring experimental data the closest to the actual conditions. Performing Hall measurements to understand the electrical properties of the materials. Finally, updating the PL system to use a diode laser for increased power level stability would improve the consistency of the PL measurements.

5.1 Alternate Radiation Types

While considering the space environment and other environments with high radiation, there are many different types of radiation that need to be considered and tested. All of these different types of radiation will affect semiconductor materials. The degree of damage that will occur and how well it anneals are two characteristics that will need to be looked into. Possible different radiation types are: heavy charged particles, fast electrons, gamma rays, and neutrons. All of these interact differently. While this paper focused on one fluence of neutron radiation, different fluences need to be examined. Using a neutron generator, as opposed to a reactor, is also recommended.

Heavy charged particles interact primarily through coulomb forces. This involves the positive charge of the heavy particle, such as an alpha particle, interacting with the negative charge of the orbital electrons within the atoms. Rutherford scattering

is another possibility, in which heavy charged particles interact with the nuclei.

Fast electrons, due to their small size, travel a very random path through an absorbing material. A much larger fraction of an electron's energy can be lost in a single encounter due to it's size. Fast electrons can cause nuclear transmutation and induce radioactivity, along with causing ionization of atoms in the material.

Gamma rays have three major types of interactions that occur. These are photoelectric absorption, Compton scattering, and pair production. These processes lead to partial or full transfer of the energy from the gamma to electron energy. This means that they do not penetrate deeply; however, they cause a lot of damage.

These different forms of radiation all need to be looked at to determine how detrimental they are to the samples, and to determine how radiation-hard the samples are.

5.2 Alternate Sn contents

Many different samples have already been grown with different tin content. The difference in the magnitude of the damage from neutron radiation (and eventually the other types of radiation mentioned in section 5.1) should be characterized. These samples, which have already been grown by Arizona State University, as well as the new structures that Dr. Yeo is working on, need to be characterized and tested. This will enable a quantitative comparison between the amount of tin concentration and the amount of damage and damage recovery after annealing in the samples.

5.3 In situ above RT annealing

While doing annealing, above room temperature, in situ measurements could be taken with the PL system so that one sample could stay under the heated conditions continuously, though the annealing temperature would be limited. This would act

similarly to how a heat pad placed under the samples would actually react to the annealing process in a true system. The PL system has the ability to be heated in the cold finger configuration. The heater could be used under vacuum to keep the sample at a set temperature while taking measurements periodically. This would require one sample to stay in the PL system continuously until annealing recovered the original PL signal. The PL system would not be able to be used for any other samples until this sample was completed. The most accurate assessment for the recovery of the PL signal would be obtained. In addition to this, different temperature annealing should be done to determine if there is a way to extrapolate the length of time for recovery of the material based on the annealing temperature. This would allow for optimization of the annealing process using the best temperature for the shortest amount of time without damaging any other material in the system.

5.4 Electrical Properties

The electrical properties of these material also need to be looked at so as to determine what has happened in the material. Therefore, Hall measurements need to be taken for these materials to determine carrier density, resistivity, and Hall mobility of the materials. This will help verify the recovery process and aid in the understanding of the underlying physical process.

VI. Conclusions

Significantly different radiation damage and recovery responses were observed in the epitaxial $Ge_{0.991}Sn_{0.009}$ material compared to the bulk Ge reference material. The direct bandgap PL signal of the Ge material showed about a 10x greater reduction in intensity than that seen in the $Ge_{0.991}Sn_{0.009}$ material following the same neutron irradiation and one week of room temperature annealing. The subsequent recovery behavior was also markedly different in the two materials. The Ge material showed a much slower rate of recovery compared to the $Ge_{0.991}Sn_{0.009}$ sample, so a linear extrapolation was used to roughly estimate expected time to full recovery; this utilized r^2 that indicates how well the data fits, with 1 being perfectly correlated and 0 having no correlation. The Ge sample at room temperature annealing has a linear extrapolated expected recovery time of 167 weeks ($r^2 = 0.8412$) for the indirect bandgap PL, and a recovery time of 80 weeks ($r^2 = 0.5209$) for the direct bandgap PL. In comparison, the 60 $°C$ annealed sample has a linear extrapolated expected recovery time of 86 weeks ($r^2 = 0.965$) for the indirect bandgap PL, and a recovery time of 26 weeks ($r^2 = 0.898$) for the direct bandgap PL. This strongly indicates that annealing at the relatively low temperature of 60 $°C$ significantly accelerates the annealing process for the germanium. Therefore, integration of a heat pad into a Ge-based system would be beneficial for annealing purposes.

After two weeks room temperature annealing, the $Ge_{0.991}Sn_{0.009}$ sample recovered approximately half of its direct bandgap PL intensity. After five weeks of room temperature annealing, the direct bandgap PL signal reached 88% of its original intensity. One of the two $Ge_{0.991}Sn_{0.009}$ samples was also exposed to 60 $°C$ annealing for 130 minutes, but unlike the behavior seen in the Ge sample, this annealing did not significantly accelerate the recovery process. Therefore, the potential benefits of integrating a heat pad with this material are inconclusive. The significantly different

radiation responses of bulk Ge and epitaxial $Ge_{0.991}Sn_{0.009}$ highlights that $GeSn$-based materials should be further researched for their neutron radiation hardness capabilities.

Appendix A. LakeShore 7704A Hall-Effect Measurement System

7700 Series/9709A Specifications

		7704A	7707A	7710A	9709A
Magnetic field	(room temp)	±1.3 T	±2 T	Please consult Lake Shore for 10 inch magnet system information	±9 T
	(variable temp)	±0.87 T	±1.2 T		±9 T
Temperature	Standard	77 K or room temperature			2 K to 400 K
	CCR	15 K to 350 K			NA
	Oven	350 K to 800 K			NA
Carrier concentration density		8×10^{2} to 8×10^{23} cm^{-3}			8×10^{2} to 8×10^{23} cm^{-3}
Mobility		1 to 1×10^{6} $cm^{2}/V\,s$			1 to 1×10^{6} $cm^{2}/V\,s$
Current (A)		±1 pA to ±100 mA			±1 pA to ±100 mA
Voltage (V)		0 V to 100 V			0 V to 100 V
Resistance range (standard)		2% accuracy— VdP minimum: 0.5 mΩ, HB minimum: 0.8 mΩ, Maximum: 100 GΩ 5% accuracy— VdP minimum: 0.1 mΩ, HB minimum: 0.04 mΩ, Maximum: 200 GΩ			2% accuracy— VdP minimum: 0.5 mΩ, HB minimum: 0.8 mΩ, Maximum: 100 GΩ 5% accuracy— VdP minimum: 0.1 mΩ, HB minimum: 0.04 mΩ, Maximum: 200 GΩ
Resistance range (AC current)		2% accuracy— VdP minimum: 10 μΩ, HB minimum: 10 μΩ, Maximum: 100 GΩ 5% accuracy— VdP minimum: 10 μΩ, HB minimum: 10 μΩ, Maximum: 200 GΩ			2% accuracy— VdP minimum: 10 μΩ, HB minimum: 10 μΩ, Maximum: 100 GΩ 5% accuracy— VdP minimum: 10 μΩ, HB minimum: 10 μΩ, Maximum: 200 GΩ
System equipment Sample holder module		75013 room temperature/77 K; 1-sided sample cards			9500-SI; 1-sided sample cards
Sample holder kit (included with sample holder module)		(1) 750SC10-50, (1) 750SC50-10, (1) 671-205, (1) 671-260, (1) 671-250, and (10) 1-inch sheets of Indium foil			Integrated into 9500-SI
Sample size		Up to 10 × 14 mm (0.4 × 0.6 in) on a 25 × 75 mm (1 × 3 in) card; up to 60 mm (2.4 in) square on an 82 × 93 mm (3.2 × 3.7 in) card	Up to 76 mm (3 in) diameter		12 × 14 mm (0.5 × 0.6 in) in a 25.4 mm (1 in) bore
Number of samples		1			1
Model 475 gaussmeter		1			NA
Model 776 matrix		1			1
Other equipment 6220 Current Source		1			1
6485 Autoranging Digital Picoammeter		1			1
2182A Digital Voltmeter		1			1

Magnet	EM4-HVA	EM7-HV		Superconducting
Pole diameter	102 mm (4 in)	178 mm (7 in)		NA
Pole face diameter	102 mm (4 in)	152 mm (6 in)	76 mm (3 in)	NA
Max magnetic field at room temperature	1.3 T (13 kG) at 25 mm (1 in) air gap	1.6 T (16 kG) at 25 mm (1 in) air gap	2.17 T (21.7 kG) at 25 mm (1 in) air gap	9 T
Max magnetic field at variable temperature	0.87 T (8.7 kG) at 51 mm (2 in) air gap	1.18 T (11.8 kG) at 51 mm (2 in) air gap	1.47 T (14.7 kG) at 51 mm (2 in) air gap	9 T
Field homogeneity	±0.1% over 10 mm^3 (0.4 in^3)	±0.1% over centered 51 mm (2 in) diameter circle		±0.1% over 60 mm (2.3 in) on axis
Cooling water requirements	Tap water or closed cycle cooling system (optional chiller available)			Liquid helium
Inlet temperature	25 °C (77 °F) maximum	32 °C (90 °F) maximum		NA
Pressure drop	200 kPa (30 psi)	220 kPa (32 psi)		NA
Flow rate	7.6 L (2 gal)/min	11.4 L (3 gal)/min		NA
Water chiller cooling capacity	2.5 kW (8,530 BTU)/h	5 kW (17,060 BTU)/h		NA
Bipolar magnet power supply	643	648		625
Mode	DC			DC
Maximum output	±35 V ±70 A (2450 W)	±75 V/±135 A (9.1 kW nominal)		±5 V/±60 A (300 W)
AC line input	204/208 VAC ±10%, 13 A/phase; 220/230 VAC ±10%, 12 A/phase; 380 VAC ±10%, 7 A/phase; 400/415 VAC ±10%, 6.5 A/phase at 50/60 Hz	200 VAC ±10%, 41 A/phase; 208 VAC ±10%, 40 A/phase; 220 VAC ±10%, 38 A/phase; 230 VAC ±10%, 37 A/phase; 380 VAC ±10%, 23 A/phase; 400 VAC ±10%, 21 A/phase; 415 VAC ±10%, 21 A/phase		Single phase 100, 120, 220, 240 VAC +6% -10%, 50 or 60 Hz, 850 VA
Flow rate	5.7 L (1.5 gal)/min minimum	7.6 L (2 gal)/min		NA
Cooling requirements	Tap water or closed cooling system (optional chiller available) +15 °C to +30 °C	Tap water or closed cooling system (optional chiller available) +15 °C to +30 °C		Air cooled
Computer	Dell® computer with HDD, CD-ROM, 19-inch SVGA flat screen monitor, Windows®, Hall software, and National Instruments IEEE-488 USB adaptor			

Model 7704A

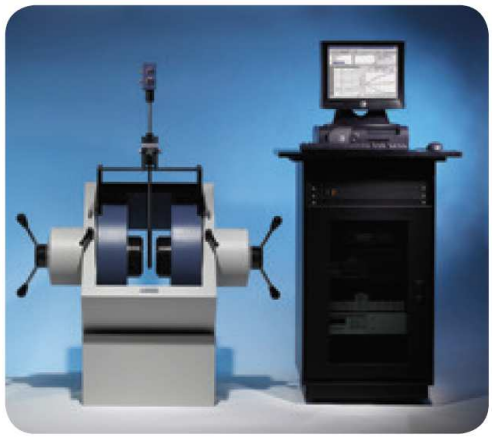

Model 7707A

Model 7610

Model 9709A

Appendix B. Photoluminescence System

2.1 Argon Ion Laser [1]

SPECTRA-PHYSICS BeamLok®
Argon Ion Laser Power Specifications

	Spectra-Physics BeamLok Argon Ion Laser Power Specifications[1]											
	λ (nm)	BeamLok 2060/65							BeamLok 2080/85			
		-4S	-5S	-6S	-7S	-8S	-10S	-10-SA	-12S	-15S	-20S	-25S
Visible Multiline Power	**454.5–514.5**	**4.0**	**5.0**	**6.0**	**7.0**	**8.0**	**10**	**10**	**12**	**15**	**20**	**25**
Visible Single-Line Power[2]	454.5	0.05	0.12	0.14	0.15	0.15	0.18	—	—	0.40	0.60	0.80
	457.9	0.25	0.35	0.42	0.45	0.55	0.55	—	—	1.2	1.4	1.5
	465.8	0.10	0.15	0.18	0.19	0.20	0.24	—	—	0.40	0.60	0.80
	472.7	0.12	0.20	0.24	0.26	0.27	0.32	—	—	0.60	1.0	1.3
	476.5	0.50	0.60	0.72	0.77	0.95	1.0	—	—	1.8	2.4	3.0
	488.0	**1.3**	**1.5**	**1.8**	**1.9**	**2.4**	**2.5**	—	—	**6.0**	**7.0**	**8.0**
	496.5	0.50	0.60	0.72	0.77	0.95	1.0	—	—	1.8	2.4	3.0
	501.7	0.30	0.40	0.48	0.51	0.54	0.64	—	—	1.0	1.4	1.8
	514.5	**1.7**	**2.0**	**2.4**	**2.6**	**3.0**	**3.2**	—	—	**7.0**	**9.0**	**10**
	528.7	0.20	0.35	0.42	0.45	0.55	0.55	—	—	1.0	1.4	1.8
Mid-UV Multiline Power[3]	**333.6–363.8**	**0.40**	**0.50**	**0.75**	**1.0**	0.30[4]	0.30[4]	0.30[4]	—	**2.0/3.0/4.0**	**4.0/5.0/6.0/7.0**	**5.0/6.0/7.0**
UV Single-Line Power[3,5]	**351.1 & 351.4**	**0.10**	**0.17**	**0.20**	**0.25**	—	—	—	—	**0.7/1.0/1.3**	**1.3/1.5/1.7/2.0**	**1.5/1.7/2.0**
	363.8	**0.10**	**0.17**	**0.20**	**0.25**	—	—	—	—	**0.7/1.0/1.3**	**1.3/1.5/1.7/2.0**	**1.5/1.7/2.0**
Other Wavelength Groups[6]	275.4–305.5	—	—	—	—	—	—	—	—	0.2/0.5/0.7	0.7/1.0/1.3/1.5	1.0/1.3/1.5
	300.3–335.8	—	—	—	—	—	—	—	—	0.5/1.0/1.5	1.5/2.0/2.5/2.7	2.0/2.5/2.7
	351.1–418.3	—	—	—	—	—	—	—	—	1.0/1.5/2.0	2.0/3.0/3.5/4.0	3.0/3.5/4.0

1. *Due to our continuous product improvement program, specifications may change without notice. All power specifications shown are in Watts.*
2. *Guaranteed power specifications for standard systems are indicated in bold print. Single-line powers are specified at 514.5 and 488.0 nm for BeamLok 2060/2080 models, and 514.5, 488.0, 351.1 and 363.8 nm for BeamLok 2065/2085 models. Power specifications for all other lines are nominal. Firm specifications for other lines require special testing and, in some cases, special optics and are only available at the time of purchase. All output power specifications, except multiline, refer to TEM_{00} (M^2<1.1) operation.*
3. *Only available with BeamLok 2065/2085 models.*
4. *Only available as an option with BeamLok 2060-8S, 2060-10S or 2060-10-SA models. Firm specifications require testing with purchased optics sets and are only available at the time of laser purchase or with plasma tube exchange.*
5. *An additional UV prism or wavelength-selective mirror (WSM) is necessary for single-line UV operation.*
6. *Only available with BeamLok 2085 models. Specifications require testing with purchased optics sets and are only available at the time of laser purchase or with plasma tube exchange.*

Spectra-Physics

Spectra-Physics
1335 Terra Bella Avenue
Mountain View, CA 94043
Tel: 1-800-775-5273
Tel: 1-(650) 961-2550
Fax: 1-(650) 964-3584
e-mail: sales@splasers.com
http://www.splasers.com

Australia: (61) 8-8443-8668
Belgium: (31) 40 265 99 59
China: (86) 10 6256 2934
France: (33) 1 6918 63 11
Germany: (49) 6151-708300
Hong Kong: (852) 2523-5688
India: (91) 80 6763 465

Israel: (972) 3-6356650
Italy: (39) 02-57465-1
Japan: Tokyo (81) 3-3794-5511
Osaka (81) 6-6941-7331
Netherlands: (31) 40 265 99 59
S. Korea: (82) 2-587-8727
Spain: (34) 91-3775006

Scandinavia: (46) 8-550 10403
Taiwan: (886) 3-426-2376
UK: (44) 1442-258100
Other European Countries:
(49) 6151-7080
Other Pacific Countries:
1-650-961-2550

CE

VISIBLE AND/OR INVISIBLE LASER RADIATION
AVOID EYE OR SKIN EXPOSURE TO DIRECT OR SCATTERED RADIATION
CLASS 4 LASER PRODUCT
ARGON/KRYPTON
MAXIMUM OUTPUT 75 W

PRINTED IN THE USA • 2/2001 • PART NUMBER 000B-0164S, REV A

Spectra-Physics BeamLok Ion Laser Beam Specifications[1]		
Output Characteristics	**BeamLok 2060/65**	**BeamLok 2080/85**
Beam Diameter[2] at $1/e^2$ points	1.7 mm	1.9 mm
Beam Divergence[2], full angle	0.45 mrad	0.45 mrad
Polarization	> 100:1 vertical	> 100:1 vertical
Cavity Length, with prism without prism	1.17 m 1.10 m	1.78 m 1.71 m
Mode Spacing, with prism without prism	133 MHz 136 MHz	84 MHz 87 MHz
Noise[3], current mode power mode 10 Hz to 500 Hz[4] 10 Hz to 2 kHz[4] 10 Hz to 20 kHz[4] 10 Hz to 2 MHz[4]	0.40% rms 0.30% rms 0.03% rms 0.05% rms 0.10% rms 0.15% rms	0.40% rms 0.30% rms 0.05% rms 0.08% rms 0.15% rms 0.20% rms
Stability[5], power mode, 8-hr period power mode, 2-hr period current mode, 8-hr period	±0.5% ±0.3% ±1.0%	±0.5% ±0.3% ±1.0%
Beam Pointing Stability[6] position offset angular offset	< 0.5 µm/°C < 5.0 µrad/°C	< 0.5 µm/°C < 5.0 µrad/°C
Single-Frequency Specifications[7]		
Temperature Range for mode-hop free operation	< 10°C	< 10°C
Frequency Drift[6,8]	< 30 MHz/°C	< 30 MHz/°C
Frequency Jitter[6,9] with J-Lok® without J-Lok	< 2 MHz < 10 MHz	< 3 MHz < 15 MHz
Conversion Efficiency[10]	> 60%	> 60%

1. *Due to our continuous product improvement program, specifications may change without notice.*
2. *Specification for 514.5 nm. For other wavelengths, assuming no change in optical configuration, the diameter is given by* $dia_1/dia_2 = \sqrt{\lambda_1/\lambda_2}$.
3. *Specification represents rms noise at 514.5 nm, measured in a 10 Hz to 2 MHz bandwidth.*
4. *Multiline (457.9–514.5 nm) performance in power mode is available with the SilentLite™ noise reduction option, which must be specified at the time of purchase.*
5. *Specification represents power stability after a 15-minute warm-up with BeamLok engaged.*
6. *Specification applies after a 30-minute warm-up with BeamLok engaged.*
7. *Specifications are for BeamLok lasers operating with the Z-Lok® single-frequency accessory package.*
8. *Z-Lok systems are capable of being locked to an external reference, such as an iodine cell. Frequency drift of <10 MHz/°C has been demonstrated with this technique.*
9. *Measured in a 10 Hz to 500 Hz bandwidth with the J-Lok jitter-reduction accessory and the cooling water flow set to the minimum required for the given laser.*
10. *Percentage of the specified* TEM_{00} *power for the given laser line.*

Spectra-Physics

2.2 Ti-Sapphire Laser [1]

Specifications

Output Characteristics[1]

Average Power[2]	675 nm[6]	700 nm	790 nm	1000 nm	1050 nm[7]
Millennia eV 10 W	800 mW	1.2 W	2.2 W	500 mW	500 mW
Millennia eV 5 W	NA	600 mW	1.0 W	250 mW	NA
Tuning Range					
Broadband Optics	700–1000 nm				
Optional X-Long Optics	950–1100 nm				
Optional Blue Optics	675–750 nm				
Linewidth Specifications					
Standard 3900S	<40 GHz				
With Thin Etalon	<15 GHz				
With Thin/Thick Etalon	<1 GHz				
Stability					
Noise[3]	<1%				
Power Drift[4]	<3%				
Beam Characteristics					
Spatial Mode	TEM00				
Polarization	>100:1 Horizontal				
Beam Diameter ($1/e^2$)[5]	0.95 mm				
Beam Divergence, full angle[5]	<1 mrad				

2.3 Preamplifier [2]

PA-9
PREAMPLIFIERS
Operating Instructions

TELEDYNE
JUDSON TECHNOLOGIES
A Teledyne Technologies Company

PB 218
January 2004

Description:

The PA-9 preamplifier is ideal for high-impedance photodiodes such as cryogenically cooled InSb, Ge and InAs. It offers superior high-frequency performance, with low current noise and ultra-low voltage noise. When ordered with a detector, the preamp is matched for maximum gain and sensitivity. Alternatively, the customer may specificy gain and/or minimum required bandwidth. Bandwidth is a function of detector resistance and capacitance as well as preamp gain, as shown on the reverse side of this bulletin.

Gain Stages:

The PA-9 has a first stage transimpedance gain and a second stage voltage gain. Output from both stages are accesable to the user.

Normal gain for the first stage is 10^7, 10^6, or 10^5 V/A. For lowest noise, choose the highest gain possible to achieve the desired bandwidth.

The second stage is set for a 10 V/V gain. Choosing 10 V/V results in lower bandwidth for the second stage. The second stage is normally AC coupled but can be DC coupled per customer specifications.

Connections:

Input and output connections are BNC feed-throughs. The power jack is a a 5-pin male Lemo connector; the mating female Lemo connector is included with the preamp.

Specifications:

Bandwidth (maximum)[1].....DC to 750 KHz

First Stage Gain.....10^7, 10^6 or 10^5 V/A

Voltage Noise Density @1 KHz..... 6.5 nV $Hz^{-1/2}$

Current Noise Density @1 KHz.....0.04 pA $Hz^{-1/2}$

Input Offset Voltage ..... ± 10 mV Typ.

Input Bias Current ..... ± 1pA Typ.

Maximum Output (First Stage).....6 V P-P
(Second Stage) .....10 V P-P

Power Requirements....±12VDC or ±15VDC, 20 mA

Size.....3" x 4.5" x 1"

[1] Using a 100K feedback resistor

Cautions:

Do not turn on the preamp power supply unless the detector is connected.

Assure that the power supply is +12V to ground and -12V to ground (NOT ± 24V).

Observe correct power supply polarity (see drawing on the reverse side of this bulletin). Improper polarity will damage the preamplifer.

PA-9 Bandwidth vs Detector Capacitance

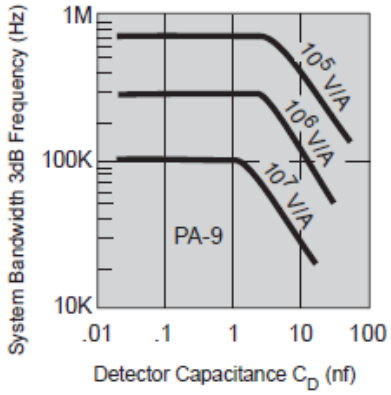

PA-9 Bandwidth vs Detector Resistance

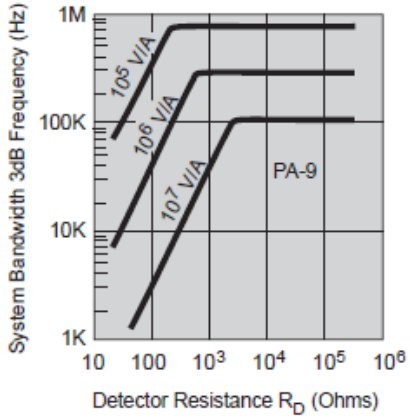

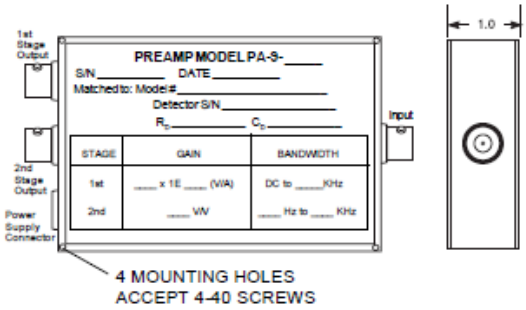

PIN	DESIGNATION
1	+12V or +15V
2	NC
3	NC
4	-12V or -15V
5	GROUND

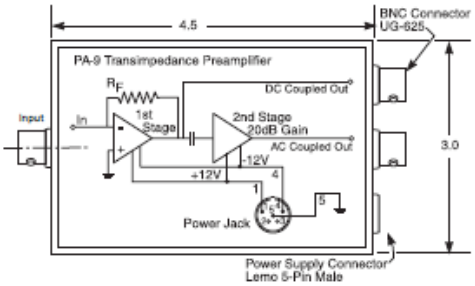

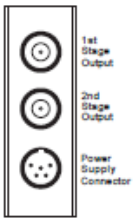

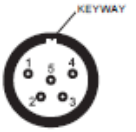

Power Supply Connector
Pin Orientation

Information in this document is believed to be reliable. However, no responsibility is assumed for possible inaccuracies or omission. Specifications are subject to change without notice.

TELEDYNE
JUDSON TECHNOLOGIES
A Teledyne Technologies Company

221 COMMERCE DRIVE
MONTGOMERYVILLE, PA 18936-9641
PHONE: 215-368-6901
FAX: 215-362-6107
www.teledynejudson.com

2/2

2.4 LakeShore 336 Temperature Controller [3]

Model 336 Cryogenic Temperature Controller

Front Panel Back Panel

Model 336 features

- Operates down to 300 mK with appropriate NTC RTD sensors
- Four sensor inputs and four independent control outputs
- Two PID control loops: 100 W and 50 W into a 50 or 25 Ω load
- Autotuning automatically collects PID parameters
- Automatically switch sensor inputs using zones to allow continuous measurement and control from 300 mK to 1505 K
- Custom display setup allows you to label each sensor input
- Ethernet, USB and IEEE-488 interfaces
- Supports diode, RTD, and thermocouple temperature sensors
- Sensor excitation current reversal eliminates thermal EMF errors for resistance sensors
- ±10 V analog voltage outputs, alarms, and relays

	AC bridge	Controllers			
	370	350	336	335	325
Number of sensor inputs	1 to 16[1]	8[1]	4	2	2
Number of user curves	20	39	39	39	15
Minimum operating temperature	<20 mK	100 mK	300 mK	300 mK	1.2 K
Maximum operating temperature	420 K	1505 K	1505 K	1505 K	1505 K
Current reversal	Yes	Yes	Yes	Yes	Yes
Current excitation autoranging	Yes	Yes	Yes	Yes	—
Number of reading displays	1 to 8	1 to 8	1 to 8	1 to 4	1 to 4
Interfaces					
Ethernet	—	Yes	Yes	—	—
USB	—	Yes	Yes	Yes	—
IEEE-488.2	Yes	Yes	Yes	Yes	Yes
RS-232C	Yes	—	—	—	Yes
Number of alarms	32	8	4	2	—
Number of relays	2	2	2	2	—
Analog voltage output	2 at ±10 V	2 at ±10 V	2 at ±10 V	1 at ±10 V	0 to 10 V
Number of autotuning control loops	1	1	2	2	2
Maximum heater output power					
Control loop 1	1 W	75 W	100 W	75 W[2]	25 W
Control loop 2	—	50 W	50 W	25 W	2 W
Number of heater ranges	8	5	3	3	2

[1] *Optional input card or scanner*
[2] *75 W only available when output 2 is in voltage mode; maximum in other modes 50 W*

2.5 F-70 Water-Cooled Compressor [4]

SHI Cryogenics Group

ABOUT US PRODUCTS APPLICATIONS SERVICE CONTACT US

F-70 Indoor Water-Cooled Compressor Series

PRODUCTS

F-70 Indoor Water-Cooled Compressor Series

RESOURCES

Cryopump Product Catalogue
Basics of Cryopumping Booklet
Cryocooler Product Catalogue
Outline Drawing

SPECIFICATIONS

	F-70L	F-70H
Electrical Supply[1]	3 Phase 200 V, 50/60 Hz	3 Phase 380–415 V, 50 Hz 480 V, 60 Hz
PowerConsumption[2]	6.6–6.9 kW at 50 Hz 7.5–7.8 kW at 60 Hz	
AmbientTemperature[3]	4–40 °C (40–104 °F)	
Cooling water (Inlet)	6–8 L/min. (1.6–2.1 gal./min.) 5–25 °C (41–77 °F)	
Dimensions(HxWxD)	532 x 443 x 493 mm (20.9 x 17.4 x 19.4 in.)	
Weight	100 kg (225 lbs.)	
Maintenance	30,000 Hours	

Home | Products | Applications | Service | Contact Us
© SHI Cryogenics Group
Site Map | Privacy | Terms of Use

Appendix C. Annealing System

Thermo Scientific Lindberg/Blue M Mini-Mite Tube Furnaces

Compact, portable single tube furnace insulated with Moldatherm for quick heatup and cooldown

- Microprocessor-based self-tuning PID control provides optimal thermal processes without overshoot
- Single segment, single setpoint, one ramp to setpoint
- Adjustable high-limit over-temperature protection
- Simultaneous LED display of temperature and setpoint in °C or °F
- Split-hinge design simplifies loading and unloading
- Safety switch disconnects power when furnace is opened
- Type K long-life thermocouple

Ordering information: Optional RS485 Digital Communications Port allows controller to be connected to a PC for remote monitoring and control of the furnace; up to 30 units can be connected to one PC. Process tubes not included and required. Purchase separately.
Includes: 9ft. (3m) power cord
Warranty[V]: 1 year (parts and labor)

NOT AVAILABLE IN EUROPE

Cat. No.	Temperature Range	Heating Zone	Outside Dia. [Tube]	Overall L x W x H	Control Temperature	Electrical	Shipping Weight
TF55030A-1	100° to 1100°C	30.5cm (12in.)	30.5cm (12in.)	28 x 41 x 38cm (11 x 16 x 15in.)	Digital, Single Segment	120V 50/60Hz 800w	16kg (35 lb.)
TF55030C-1	100° to 1100°C	30.5cm (12in.)	30.5cm (12in.)	28 x 41 x 38cm (11 x 16 x 15in.)	Digital, Single Segment	208/240V 50/60Hz 800w	16kg (35 lb.)
TF55035A-1	100° to 1100°C	30.5cm (12in.)	30.5cm (12in.)	28 x 41 x 38cm (11 x 16 x 15in.)	Digital, Multisegment Programmable	120V 50/60Hz 800w	16kg (35 lb.)
TF55035C-1	100° to 1100°C	30.5cm (12in.)	30.5cm (12in.)	28 x 41 x 38cm (11 x 16 x 15in.)	Digital, Multisegment Programmable	208/240V 50/60Hz 800w	16kg (35 lb.)

Bibliography

1. Spectra-physics.com, "Spectra-Physics," 2016. [Online]. Available: http://www.spectra-physics.com/

2. Judsontechnologies.com, "Teledyne Judson Technologies: Preamplifiers," 2016. [Online]. Available: http://judsontechnologies.com/preamp.html

3. Lakeshore.com, "Model 336 — Overview — Lake Shore Cryotronics, Inc." 2016. [Online]. Available: http://www.lakeshore.com/products/cryogenic-temperature-controllers/model-336/pages/Overview.aspx

4. Shicryogenics.com, "F-70 Indoor Water-Cooled Compressor Series - SHI Cryogenics Group," 2016. [Online]. Available: http://www.shicryogenics.com/products/compressors/f-70-indoor-water-cooled-compressor-series/

5. M. D. Hamilton, "Electrical and Optical Characterization of Si-Ge-Sn," Master's thesis, AIR FORCE INST OF TECH WRIGHT-PATTERSON AFB OH SCHOOL OF ENGINEERING AND MANAGEMENT/DEPT OF ENGINEERING PHYSICS, 3 2012, iD: 794273169.

6. J. Mathews, R. Roucka, J. Xie, S.-Q. Yu, J. Menndez, and J. Kouvetakis, "Extended performance GeSn/Si (100) pin photodetectors for full spectral range telecommunication applications," *Applied Physics Letters*, vol. 95, no. 13, p. 133506, 2009.

7. T. R. Harris, "A Systematic Study of the Optical and Electrical Properties of $Ge_{1-y}Sn_y$ and $Ge_{1-x-y}Si_xSn_y$ Semiconductor Alloys," Ph.D. dissertation, AIR FORCE INST OF TECH WRIGHT-PATTERSON AFB OH SCHOOL OF ENGINEERING AND MANAGEMENT/DEPT OF ENGINEERING PHYSICS, 3 2014.

8. M. E. Levinshtein, S. L. Rumyantsev, and M. Shur, *Handbook series on semiconductor parameters*. World Scientific, 1996.

9. T. R. Harris, Y. K. Yeo, M.-Y. Ryu, R. T. Beeler, and J. Kouvetakis, "Observation of heavy- and light-hole split direct bandgap photoluminescence from tensile-strained GeSn (0.03% Sn)," *Journal of Applied Physics*, vol. 116, no. 10, p. 103502, 2014.

10. M. Kira and S. W. Koch, "Many-body correlations and excitonic effects in semiconductor spectroscopy," *Progress in Quantum Electronics*, vol. 30, no. 5, pp. 155–296, 2006.

11. M. Lindberg and S. W. Koch, "Effective Bloch equations for semiconductors," *Phys.Rev.B*, vol. 38, no. 5, pp. 3342–3350, Aug 1988. [Online]. Available: http://link.aps.org/doi/10.1103/PhysRevB.38.3342

12. G. Leman, *Annales de Physiques*, 7th ed., 1962.

13. D. J. Griffiths, *Introduction to Electrodynamics*. Prentice Hall, 1999, 98050525. [Online]. Available: https://books.google.com/books?id=M8XvAAAAMAAJ

14. R. F. Pierret, *Semiconductor device fundamentals*. Addison-Wesley, 1996. [Online]. Available: https://books.google.com/books?isbn=0131784595

15. N. Carron, *Passage of Energetic Particles Through Matter*. Ft. Belvoir Defense Technical Information Center, 3 2003.

16. R. Aluguri, S. Manna, and S. K. Ray, "Direct band gap optical emission from compressively strained Ge films grown on relaxed Si0.5Ge0.5 substrate," *Applied Physics Letters*, vol. 103, no. 16, p. 161118, 10/14 2013. [Online]. Available: http://search.ebscohost.com/login.aspx?direct=true&db=inh&AN=13830899&site=ehost-live

17. H. W. Kraner, R. H. Pehl, and E. E. Haller, "Fast Neutron Radiation Damage of High-Purity Germanium Detectors," *Nuclear Science, IEEE Transactions on*, vol. 22, no. 1, pp. 149–159, 1975, iD: 1.

18. I. Pelant and J. Valenta, *Luminescence Spectroscopy of Semiconductors*. OUP Oxford, 2012, 2012931995. [Online]. Available: https://books.google.com/books?id=CqD5HjFyWsMC

19. S. Dun, T. Lu, Q. Hu, Y. Hu, C. You, S. Zhang, B. Tang, J. Dai, and N. Huang, "Photoluminescence study of Ge nanocrystals irradiated by reactor neutron flux," *Nuclear Instruments and Methods in Physics Research Section B: Beam Interactions with Materials and Atoms*, vol. 264, no. 2, pp. 272–276, 11 2007.

20. A. Holmes-Siedle and L. Adams, *Handbook of Radiation Effects*, 2nd ed. OUP Oxford, 2002.

21. G. S. Hubbard and E. E. Haller, "The Influence of Material Parameters on Fast Neutron Radiation Damage of High Purity Germanium Detectors," *Nuclear Science, IEEE Transactions on*, vol. 27, no. 1, pp. 235–239, 1980, iD: 1.

22. G. L. Keister and H. V. Stewart, "The Effect of Nuclear Radiation on Selected Semiconductor Devices," *Proceedings of the IRE*, vol. 45, no. 7, pp. 931–937, 1957, iD: 1.

23. G. S. Was, *Fundamentals of Radiation Materials Science: Metals and Alloys*. Springer Berlin Heidelberg, 2007. [Online]. Available: https://books.google.com/books?id=0N06swAJI0AC

24. Nature.berkeley.edu, "sect24," 2016. [Online]. Available: http://nature.berkeley.edu/~penggong/textbook/chapter2/html/sect24.htm

25. S. Mathimalar, N. Dokania, V. Singh, V. Nanal, R. G. Pillay, A. Shrivastava, K. C. Jagadeesan, and S. V. Thakare, "Study of radioactive impurities in neutron transmutation doped germanium," *Nuclear Instruments and Methods in Physics Research Section A: Accelerators, Spectrometers, Detectors and Associated Equipment*, vol. 774, pp. 68–73, 2/21 2015.

26. G. Messenger and M. Ash, *The effects of radiation on electronic systems.* New York: Van Nostrand Reinhold Co., 1986.

27. T. Ross, C. Beausang, I. Lee, A. Macchiavelli, S. Gros, M. Cromaz, R. Clark, P. Fallon, H. Jeppesen, and J. Allmond, "Neutron damage tests of a highly segmented germanium crystal," *Nuclear Instruments and Methods in Physics Research Section A: Accelerators, Spectrometers, Detectors and Associated Equipment*, vol. 606, no. 3, pp. 533–544, 2009.

28. H. Spieler, "Introduction to radiation-resistant semiconductor devices and circuits," in *AIP Conference Proceedings.* IOP INSTITUTE OF PHYSICS PUBLISHING LTD, 1997, pp. 23–49.

REPORT DOCUMENTATION PAGE

Form Approved
OMB No. 0704–0188

The public reporting burden for this collection of information is estimated to average 1 hour per response, including the time for reviewing instructions, searching existing data sources, gathering and maintaining the data needed, and completing and reviewing the collection of information. Send comments regarding this burden estimate or any other aspect of this collection of information, including suggestions for reducing this burden to Department of Defense, Washington Headquarters Services, Directorate for Information Operations and Reports (0704–0188), 1215 Jefferson Davis Highway, Suite 1204, Arlington, VA 22202–4302. Respondents should be aware that notwithstanding any other provision of law, no person shall be subject to any penalty for failing to comply with a collection of information if it does not display a currently valid OMB control number. **PLEASE DO NOT RETURN YOUR FORM TO THE ABOVE ADDRESS.**

1. REPORT DATE *(DD–MM–YYYY)*	2. REPORT TYPE	3. DATES COVERED *(From — To)*
24–03–2016	Master's Thesis	June 2015 - March 2016

4. TITLE AND SUBTITLE

Neutron Radiation Effects on Ge and GeSn semiconductors

5a. CONTRACT NUMBER

5b. GRANT NUMBER

5c. PROGRAM ELEMENT NUMBER

6. AUTHOR(S)

O'Daniel, Christopher T., 2d Lt, USAF

5d. PROJECT NUMBER

5e. TASK NUMBER

5f. WORK UNIT NUMBER

7. PERFORMING ORGANIZATION NAME(S) AND ADDRESS(ES)

Air Force Institute of Technology
Graduate School of Engineering and Management (AFIT/EN)
2950 Hobson Way
WPAFB OH 45433-7765

8. PERFORMING ORGANIZATION REPORT NUMBER

AFIT-ENP-MS-16-M-077

9. SPONSORING / MONITORING AGENCY NAME(S) AND ADDRESS(ES)

Air Force Office of Scientific Research
AFOSR/RTA
POC: Dr. Gernot S. Pomrenke (gernot.pomrenke@us.af.mil)
8725 North Randolph Street
Arlington, Virginia 22203-1768

10. SPONSOR/MONITOR'S ACRONYM(S)

AFOSR/RTA

11. SPONSOR/MONITOR'S REPORT NUMBER(S)

12. DISTRIBUTION / AVAILABILITY STATEMENT

Distribution Statement A. Approved for public release; Distribution Unlimited.

13. SUPPLEMENTARY NOTES

This material is declared work of the U.S. Government and is not subject to copyright protection in the United States.

14. ABSTRACT

Two different semiconductor materials received neutron radiation for assessment of radiation damage. The two materials are undoped bulk Ge and epitaxial $Ge_{0.991}Sn_{0.009}$, which is doped heavily with phosphorous. At room temperature, the Ge sample has direct and indirect bandgaps at 0.78 eV and 0.66 eV, respectively. The $Ge_{0.991}Sn_{0.009}$ sample has direct and indirect bandgaps at 0.72 eV and 0.63 eV, respectively. Two samples of each material were exposed to research reactor neutrons, delivering a 1 MeV equivalent neutron fluence of $2.52 \times 10^{15}\ \frac{n}{cm^2}$. In order to assess the radiation damage and recovery, photoluminescence (PL) measurements were taken before and after irradiation weekly. The Ge experienced heavy neutron radiation damage, decreasing the direct and indirect bandgap PL intensity to about 4% and 1%, respectively, from the pre-neutron irradiation value. Room temperature annealing of the Ge sample over four weeks brought the recovery of the direct and indirect bandgap PL intensities only to about 7% and 3%, while an accumulated 60 $°C$ annealing for 100 minutes brought the PL recoveries to about 11% and 3%, respectively. The $Ge_{0.991}Sn_{0.009}$ sample experienced neutron damage that decreased the direct bandgap PL intensity to about 37% of the pre-neutron irradiation PL intensity. The direct bandgap PL intensities recovered to 88% and 86%, respectively after five weeks for a sample annealed only at room temperature and a sample that was also annealed at 60 $°C$ for 130 minutes. The significantly different radiation responses of bulk Ge and epitaxial $Ge_{0.991}Sn_{0.009}$ highlights that $GeSn$-based materials should be further researched for their neutron radiation hardness capabilities.

15. SUBJECT TERMS

Ge, GeSn, Neutron Radiation, Absorption, Photoluminescence, Valence Band

16. SECURITY CLASSIFICATION OF:			17. LIMITATION OF ABSTRACT	18. NUMBER OF PAGES	19a. NAME OF RESPONSIBLE PERSON
a. REPORT	b. ABSTRACT	c. THIS PAGE			Dr. Yung Kee Yeo, AFIT/ENP
U	U	U	UU	79	19b. TELEPHONE NUMBER *(include area code)* (937)255-3636 x.4532; Yung.Yeo@afit.edu